Nucleic Acids Research, 2024, **52**, 1878–1895
https://doi.org/10.1093/nar/gkad1210
Advance access publication date: 28 December 2023
Nucleic Acid Enzymes

Molecular mechanism of human ISG20L2 for the ITS1 cleavage in the processing of 18S precursor ribosomal RNA

Yinliang Ma[1,†], Jiaxu Wang[1,2,†], Xingyi He[1], Yuhang Liu[1], Shuo Zhen[1], Lina An[1], Qian Yang[1], Fumin Niu[1], Hong Wang[1], Boran An[3], Xinyue Tai[1], Zhenzhen Yan[1], Chen Wu[1,*], Xiaoyun Yang[1,4,*] and Xiuhua Liu[1,*]

[1]College of Life Sciences, Hebei Innovation Center for Bioengineering and Biotechnology, Institute of Life Sciences and Green Development, Hebei University, Baoding 071002 Hebei, China
[2]College of Life Sciences, State Key Laboratory of Cell Differentiation and Regulation, Henan International Joint Laboratory of Pulmonary Fibrosis, Henan Normal University, Xinxiang 453002 Henan, China
[3]Affiliated Hospital of Hebei University, Hebei University, Baoding 071002 Hebei, China
[4]Department of Biology, Southern University of Science and Technology, Shenzhen 518055 Guangdong, China

[*]To whom correspondence should be addressed. Tel: +86 13315235028; Fax: +86 03125079364; Email: liuxiuhua_2004@163.com
Correspondence may also be addressed to Xiaoyun Yang. Tel: +86 13051577101; Email: xiaoyun_y90@163.com
Correspondence may also be addressed to Chen Wu. Tel: +86 13903129899; Fax: +86 03125079364; Email: wuchen@hbu.edu.cn
[†]The first two authors should be regarded as Joint First Authors.

Abstract

The exonuclease ISG20L2 has been initially characterized for its role in the mammalian 5.8S rRNA 3′ end maturation, specifically in the cleavage of ITS2 of 12S precursor ribosomal RNA (pre-rRNA). Here, we show that human ISG20L2 is also involved in 18S pre-rRNA maturation through removing the ITS1 region, and contributes to ribosomal biogenesis and cell proliferation. Furthermore, we determined the crystal structure of the ISG20L2 nuclease domain at 2.9 Å resolution. It exhibits the typical αβα fold of the DEDD 3′-5′ exonuclease with a catalytic pocket located in the hollow near the center. The catalytic residues Asp[183], Glu[185], Asp[267], His[322] and Asp[327] constitute the DEDDh motif in ISG20L2. The active pocket represents conformational flexibility in the absence of an RNA substrate. Using structural superposition and mutagenesis assay, we mapped RNA substrate binding residues in ISG20L2. Finally, cellular assays revealed that ISG20L2 is aberrantly up-regulated in colon adenocarcinoma and promotes colon cancer cell proliferation through regulating ribosome biogenesis. Together, these results reveal that ISG20L2 is a new enzymatic member for 18S pre-rRNA maturation, provide insights into the mechanism of ISG20L2 underlying pre-rRNA processing, and suggest that ISG20L2 is a potential therapeutic target for colon adenocarcinoma.

Graphical abstract

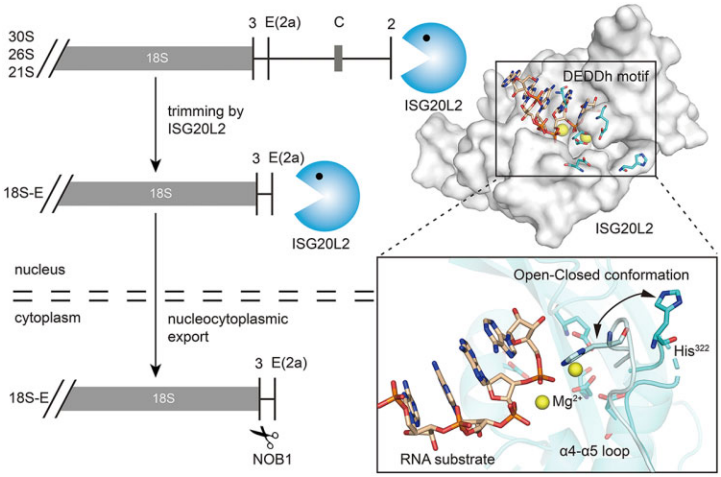

Introduction

The eukaryotic ribosome biogenesis is a complex, multi-step process, and contains a series of tightly controlled events, including ribosomal DNA (rDNA) transcription, extensive processing of precursor ribosomal RNA (pre-rRNA) into mature rRNA, and the final assembly of these molecules with

Received: November 22, 2022. **Revised:** December 3, 2023. **Editorial Decision:** December 6, 2023. **Accepted:** December 10, 2023

ribosomal proteins to form mature ribosomes (1). The ribosome biosynthesis is under precise temporal and spatial controls, and is coupled to cellular growth rate, their abnormalities are often associated with genetic diseases and cancer in humans (2–6).

The mature human ribosome (80S) is composed of the large 60S (LSU) and 40S (SSU) subunits, both of which contain about 50 and 30 proteins, respectively (1,7). Each subunit contains different rRNA species. The LSU contains 5S, 5.8S and 28S rRNAs, and the SSU contains 18S rRNA (7). To initiate the ribosome synthesis in human cells, RNA polymerase I transcribes rDNA into a huge polycistronic 47S pre-rRNA molecule containing 18S, 5.8S and 28S rRNA, as well as the external and internal transcribed spacer regions (5′-ETS, ITS1, ITS2 and 3′-ETS) (Figure 1A) (2). Subsequently, the long pre-RNA is systematically cleaved by ribonucleases to generate mature 18S, 5.8S and 28S rRNA in human cells, meanwhile, RNA polymerase III is independently responsible for the synthesis of 5S rRNA (1,8).

A series of exonucleolytic and endonucleolytic processing steps are involved in the removal of transcribed spacers (3,6). After removal of 3′-ETS and processing in 5′-ETS, cleavages within ITS1 release the precursors of 18S rRNA and the other precursor consisting of 5.8S, ITS2 and 28S rRNAs. And subsequent cleavages at site 4 within ITS2 generate the precursors of 5.8S and 28S rRNAs respectively, which are further processed under the action of exonucleases to eliminate excised spacer fragments and generate mature rRNA ends (1,9).

ITS1 removal is a significant event in ribosome maturation, and leads to the segregation of the 47S functional precursor into rRNA elements of SSU and LSU (1,6). Two cleavage sites were identified in the ITS1 region in human cells: sites E(2a) and 2. Both cleavage sites are utilized in human ITS1 processing, generating two alternative processing pathways, to form functional 18S precursors (1,10). Cleavage at distal site 2 occurs more frequently and is predominantly independent of the removal of 5′-ETS, consequently generating diverse precursors of 18S rRNA with different 5′-ends (30S, 26S and 21S) and 32S pre-rRNA, the precursors of 5.8S and 28S rRNAs (1). Alternatively, cleavage at proximal site E(2a) under the action of endonuclease UTP24 represents the minority pathway, and solely occurs after the full removal of 5′-ETS, generating the precursor 18S-E(2a) (1,6,11,12). Generally, after cleavage at site 2 in human cells, these 18S pre-rRNA species (30S, 26S and 21S) are further processed by exosome-mediated exonucleolytic digestion (more especially by RRP6) or UTP24-mediated endonucleolytic cleavage at site E(2a), releasing the 18S-E(2a) pre-rRNA (1,6,11,12).Then, the poly(A) ribonuclease (PARN) is involved in 3′-5′ cleavage of 18S-E(2a) pre-rRNA in the nucleus, facilitating the nucleocytoplasmic export of the 18S-E(2a) (13). And the endonuclease NOB1 contributes to the final processing of the 3′ end of 18S pre-rRNA in the cytoplasm (6,12,14). Although considerable progress has been made in human ribosome biogenesis, the mechanistic understanding of the ribosomal RNA processing pathways is still missing, including the identification of all ribonucleases contributed to the processing of diverse pre-rRNA intermediates (13).

Interferon-stimulated 20-kDa exonuclease-like 2 (ISG20L2) is a nucleolar exonuclease and belongs to the DEDD 3′-5′ exonuclease superfamily, which is divided into DEDDy and DEDDh two groups (15,16). Human ISG20L2 is a member of the DEDDh subfamily. Although vertebrate exonucleases Rex4, ISG20, ISG20L1, and ISG20L2 are the co-orthologs of *Saccharomyces cerevisiae* Rex4, which is involved in the *S. cerevisiae* ITS1 cleavage and ribosome biogenesis (1,17,18), they perform different biological functions. Specifically, human ISG20 is closely related to host antiviral innate immune defense (19,20), and may be involved in tumorigenesis and progression of neoplasms (21). Human Rex4 is required for transcriptional regulation of the quinone reductase gene and removal of estrogen-induced abasic sites in DNA (22,23). And human ISG20L1 mediates p53-induced apoptosis (24,25).

Human ISG20L2 contains an N-terminal disorder region (residues 1-177) and a C-terminal functional DEDD domain (residues 178-353), exerting the exonuclease activity on RNAs. It has been reported that ISG20L2 is involved in the 5.8S rRNA maturation, functioning redundantly with several exoribonucleases in the cleavage of ITS2 of 12S pre-rRNA (17). Here, we found that ISG20L2 is also involved in 18S pre-rRNA maturation by cleaving the ITS1 regions of 30S, 21S and 18S-E pre-rRNAs. And we carried out structural and biochemical studies to demonstrate the mechanistic basis of ISG20L2 for pre-rRNA processing. Finally, cellular assays revealed that ISG20L2 promotes colon cancer cell growth through its nuclease activity. Together, our results reveal that ISG20L2 is a new enzymatic member for the 18S pre-rRNA maturation, provide insights into the molecular mechanism of ISG20L2 for pre-rRNA processing, and suggest that ISG20L2 is a potential anti-cancer target for colon adenocarcinoma in future.

Materials and methods

Cell culture, antibodies, siRNA and plasmid

HEK-293T, HCT116, NCM460, SW480, SW620 and HT29 cell lines were maintained in DMEM medium supplemented with 10% FBS in a humidified incubator with 5% CO_2 at 37°C. The primary antibodies were used as follows: anti-ISG20L2 antibody (24639-1-AP, Proteintech), anti-GAPDH antibody (60004-1-Ig, Proteintech), anti-DDDDK-tagged antibody (M185-3L, MBL), anti-PARN antibody (13799-1-AP, Proteintech), anti-NOB1 antibody (10091-2-AP, Proteintech), anti-DIS3 antibody (14689-1-AP, Proteintech), anti-CyclinB1 antibody (4138, Cell Signaling), anti-CDK1 antibody (19532-1-AP, Proteintech), anti-p53 antibody (60283-2-AP, Proteintech), anti-p21 antibody (ab109520, Abcam).

Different siRNAs that used to knockdown expression of the human rRNA processing factor genes were listed as follows: PARN (GenBank accession number: NM_002582.4): 5′-GCUCCAGCAUUGACUUUCUdTdT-3′ (siPARN); NOB1 (GenBank accession number: NM_014062.3): a mixture of 5′-CGCCCUGGAGCCAAUCUUCAAdTdT-3′ (siNOB1-1Q), 5′-UUGCCCAACAUCGAUCAUGAAdTdT-3′ (siNOB1-2Q) and 5′-GGUUAAGGUGAGCUCAUCGdTdT-3′ (siNOB1-3); DIS3 (GenBank accession number: NM_014953.5): 5′-AGGUAGAGUUGUAGGAAUAdTdT-3′ (siDIS3). Cells were transfected with the indicated siRNA duplexes (working concentration: 50 nM) using Lipofectamine™ 2000 (Invitrogen, CA, USA). The cells were harvested after 72 h transfection, and then analyzed for Western and Northern blots.

For all complementation assays, the full length of ISG20L2 wild-type and mutations (H322A and M186A/R226A/W229A) were cloned into the modified

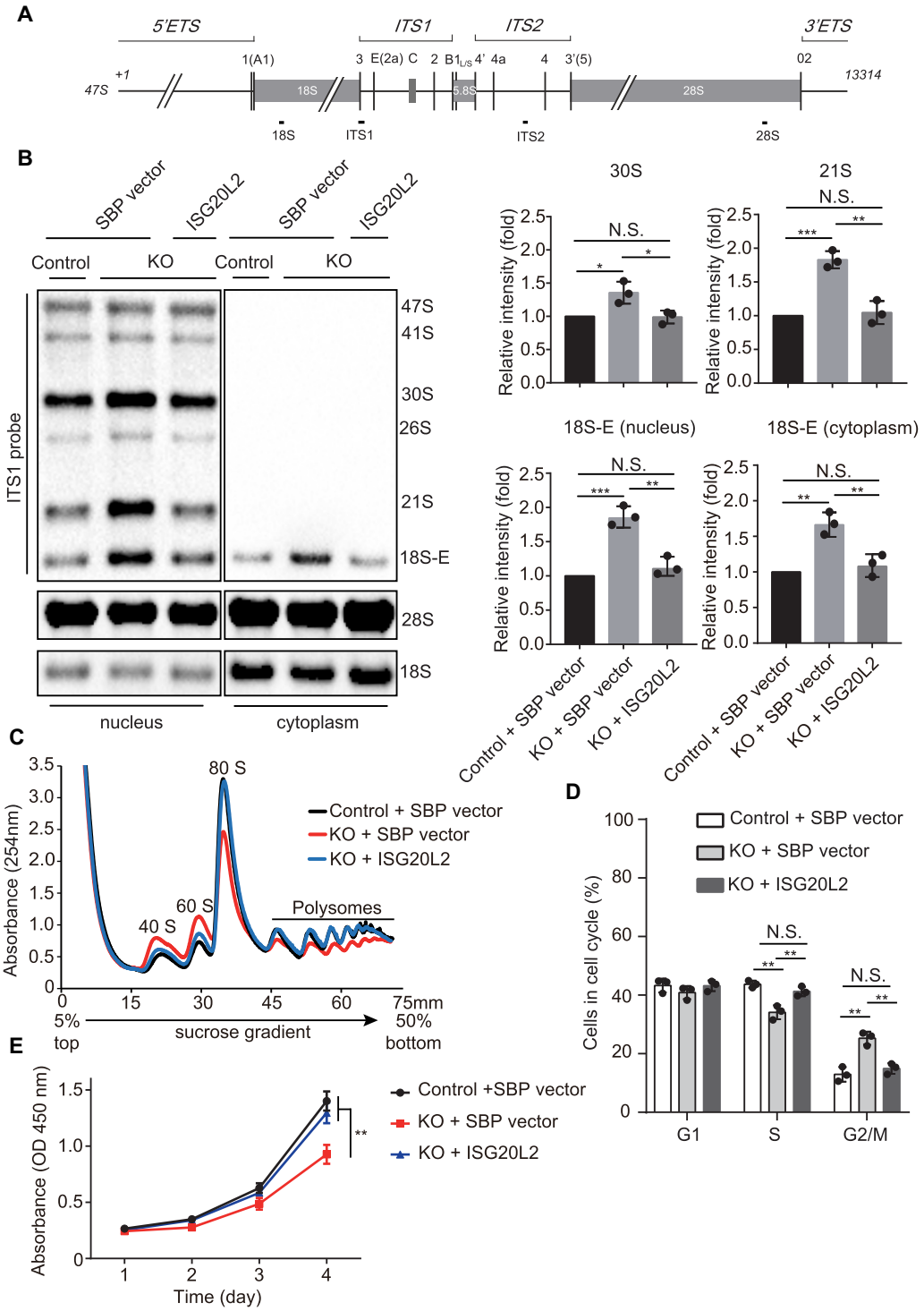

Figure 1. Human ISG20L2 participates in the ITS1 progressing. (**A**) Schematic representation of 47S pre-rRNA. The processing or cleavage sites in both ITS1 and ITS2 regions are displayed with vertical thin lines together with the names. The black bars below the pre-rRNA indicate the relative positions of Northern blot probes used in this study. (**B**) Nuclear and cytoplasmic RNA was extracted from ISG20L2-KO HEK-293T cells, ISG20L2-KO cells transfected with ISG20L2 plasmid, or control cells respectively, and then analyzed by Northern blot. The nylon transfer membrane was hybridized with 28S, ITS1, and 18S probes, respectively. Representative Northern blots of the various 18S pre-rRNA intermediates detected were indicated in the left panel. The bar diagrams (right panel) show the quantification of the processing intermediate levels normalized to the 28S rRNA; the values of 30S, 21S, and 18S-E pre-rRNAs from HEK-293T control cells were set to 1, respectively. The quantification schemes are followed for all figures. Mean ± SD, $n = 3$. $^{*}P < 0.05$; $^{**}P < 0.01$; $^{***}P < 0.001$; N.S., no significance. SBP vector: the modified pIRES2-EGFP vector containing two FLAG-tag, one S-tag and one Streptavidin-Binding Peptide (SBP)-tag. (**C**) The polyribosome profile analysis was detected by the absorbance at 254 nm on 5-50% sucrose gradient. ISG20L2-KO cells represented increased ratios of individual subunits (40S and 60S) and decreased ratios of monosome (80S) and polysomes. The imbalanced polyribosome profile was restored by the re-expression of ISG20L2 in ISG20L2-KO cells. (**D**) The cell cycle of HEK-293T cell was analyzed by Flowcytometry. ISG20L2 depletion arrests cells in the G2/M-phase and also causes a reduction in S-phase cells. Reconstitution of ISG20L2 protein restored the cell cycle arrest in ISG20L2-KO cells. Mean ± SD, $n = 3$. $^{**}P < 0.01$; N.S., no significance. (**E**) CCK8 assays were used to detect the effect of ISG20L2 depletion on cell proliferation. Mean ± SD, $n = 3$. $^{**}P < 0.01$.

pIRES2-EGFP vector (termed SBP vector) containing two FLAG-tags, one S-tag and one Streptavidin Binding Peptide (SBP)-tag.

Establishment of stable cell line

The sgRNA targeting ISG20L2 was designed from CRISPR DESIGN (http://crispr.mit.edu/), and cloned into pSpCas9 (BB)-2A-Puro (PX459) V2.0. The sequence used for knockout (KO) was as follows: GGGGAAACTCCTACGGTCGA. HEK-293T cells were transfected with ISG20L2-PX459 KO plasmid according to Lipofectamine™ 2000 (Invitrogen, CA, USA) instruction. Stable transfectants of ISG20L2-KO were screened by puromycin (2.5 μg/ml) for one week. The ISG20L2-KO cell lines were confirmed by Western blot.

To generate the full length of ISG20L2 wild-type and mutations (D183A, E185A, D267A, D327A, H322A, M186A, R226A, W229A and M186A/R226A/W229A) overexpression (OE) plasmids, the optimized ISG20L2 open reading frames (Supplementary Table S1) (GenScript, China) were cloned into the modified pCDH-EF1-SFP-IRES2-Puro (pESIP) vector containing two FLAG-tag, one S-tag and one Streptavidin Binding Peptide (SBP)-tag. These mutations were designed based on the crystal structure of ISG20L2 and sequence conservation analysis. The Amplification primers are listed in Supplementary Table S2. The lentivirus system was used for ISG20L2 OE stable cell lines screening. For lentivirus production, the HEK-293T cells were transfected with the recombinant plasmid, pxPAX2 and pMD2.G plasmids. After 48 h of incubation, the packaged virus was used to infect HEK-293T cells. The stable ISG20L2 OE cell lines were selected with 2.5 μg/ml puromycin.

The sequences used for ISG20L2 knockdown (KD) shRNA1: CCGGGGAAATGCCAAGCACCGAAATCTC GAGATTTCGGTGCTTGGCATTTCCTTTTTG; ISG20L2 KD shRNA2: CCGGGCCTAAGTTGCACTCTGAACCC TCGAGGGTTCAGAGTGCAACTTAGGCTTTTTG. Both shRNA1 and shRNA2 were cloned into the pLKO1 vector, respectively. Similar to the protocol for ISG20L2 OE stable cell line construction, SW480 cells were transfected with shRNA1-pLKO1 or shRNA2-pLKO1, pxPAX2 and pMD2.G plasmids. Puromycin (2.5 μg/ml) was used for ISG20L2 KD cell lines screening.

Western blot

Cells were lysed with NETN420 buffer (50 mM Tris-HCl, pH 7.5, 420 mM NaCl, 2 mM EDTA, 1% Nonidet P-40, 100 mM PMSF and 0.5 mM DTT). The equal amounts of the whole cell lysate were separated by 12% SDS-PAGE and transferred to polyvinylidene difluoride (PVDF) membrane, then blocked with 5% skimmed milk in TBST buffer and finally probed with specific primary antibodies. The blots were visualized with an enhanced chemiluminescence kit and imaged using ChemiDoc™ MP Imaging System (Bio-Rad, CA, USA).

Immunofluorescence

The cells were seeded onto coverslips and fixed with 4% paraformaldehyde for 15 min. And then 0.5% Triton X-100 was used for permeabilize the cells for 15 min. Subsequently, the cells were blocked with 8% goat serum in PBS for 30 min, and incubated with ISG20L2 antibody (dilution: 1:100) overnight at 4°C. Then the cells were incubated with secondary antibody Alexa Fluor™ 488, goat anti-rabbit IgG (1:400, A11034, Invitrogen) for 1 h in the dark. The nuclei were then stained by DAPI (Beyotime, China) for 3 min. Cells were visualized with a fluorescence microscope (IX73, Olympus).

Protein purification from HEK-293T OE cells

The ISG20L2 wild-type or ISG20L2-mutation OE cells were lysed with NETN420 buffer for 15 min. The fractions were harvested after centrifugation and diluted with a two-folded volume of NETN0 (50 mM Tris-HCl, pH 7.5, 1% Nonidet P-40, 100 mM PMSF), then incubated Streptavidin Agarose Beads (Invitrogen, IL, USA) for 4 h at 4°C. The beads were washed five times, and the fusion proteins were eluted from beads with 2 mg/ml biotin. Subsequently, biotin was removed by dialysis buffer (50 mM Tris-HCl, pH 7.5, 200 mM NaCl). All buffers mentioned above were prepared using RNase-free deionized water. The eluent containing ISG20L2 wild-type or mutant proteins was stored for the subsequent exonuclease assays *in vitro* and thermal shift assays.

RNA extraction

Cells were lysed using NETN100 buffer (25 mM Tris-HCl pH 7.5, 100 mM NaCl, 0.5% Nonidet P-40, 1 U/μl RNase inhibitor, 100 mM PMSF) (26,27). The lysate was centrifuged at 2000 g at 4°C for 20 min to separate the NETN100 soluble and pellet fractions. Then both fractions were respectively used to extract RNA using Trizol reagent based on the manufacturer's instructions (Invitrogen, CA, USA). The RNA was stored at -80°C.

Northern blot analysis

One microgram of RNA extracted from NETN100 pellets or three micrograms of RNA extracted from NETN100 soluble fraction was respectively separated on 1% formaldehyde agarose gels and transferred into a nylon transfer membrane (GE Healthcare, UK) using 20× SSC (0.3 M sodium citrate; 3 M sodium chloride). After UV cross-linking, the membrane pre-hybridization was carried out at 42°C in a hybridization buffer (Invitrogen, Lithuania). The 5′-biotin labeled oligonucleotide probe was added after 3 h and incubated overnight at 42°C. The sequences of all the probes are as follows: U6 snRNA: ATATGGAACGCTTCACGAATT; ct-tRNA^{Lys}: CGCCTGAACAGGGACTTGAACCCTGGACCC; 18S: ACGGCGACTACCATCGAAAG; 28S: AACGATCAGA GTAGTGGTATTTCACC; ITS1: CCTCGCCCTCCGGGCT CCGTTAATGATC; ITS2: GCGCGACGGCGGACGACACC GCGGCGTC. The signals were visualized with the Chemiluminescent Nucleic Acid Detection Module Kit (Thermo Fisher, IL, USA) and imaged using ChemiDoc^{TM} MP Imaging System (Bio-Rad, CA, USA).

Polyribosome profile analysis

Before collection, cells were incubated with 100 μg/ml cycloheximide (CHX) for 10 min. Then 3 × 10^7 cells were collected, washed twice using the cold PBS buffer containing 100 μg/ml CHX and resuspended with 500 μl lysis buffer (10 mM Tris-HCl, pH 7.5, 2.5 mM $MgCl_2$, 1.5 mM KCl, 1 mM DTT, 1% Triton X-100, 0.5% Na-Deoxycholate, 1 × protease inhibitor cocktail (EDTA-free), 100 U/ml RNase inhibitor, 100 μg/ml CHX) and lysed using vortex for 5 s. After centrifugation at 13 000 rpm for 15 min at 4°C, 400 μl of

extractions equal to 15-20 OD_{260} units were layered onto a linear 5-50% sucrose gradient. The samples were centrifuged at SW41Ti rotor (Beckman Coulter) for 2 h at 36 000 rpm at 4°C. The gradients were measured by gradient station (Biocomp).

Cell cycle and cell proliferation analysis

1×10^6 cells were cultured and digested by trypsin (with EDTA), then washed twice using PBS, and the harvested cells were fixed in 70% ethanol. After storage at -20°C overnight, the fixed cells were washed three times using PBS and treated with 100 μg/ml RNase A (DNase-free) for 30 min at 37°C, then stained with 50 μg/ml propidium iodide (PI; Sigma) for 30 min. Cells were run on Flow Cytometry (Beckman, CA, USA), and cell cycle analysis was carried out by FlowJo7.6 software. The experiment was independently repeated three times.

Cell proliferation was measured using the Cell Counting Kit-8 (K1018, Apexbio, USA) according to the manufacturer's instructions. Cells were harvested and seeded onto 96-well plates (1000 cells per well per 100 μl). Then the cells were cultured for 24 h at the incubator, and 10 μl CCK8 reagent was added into each well and incubated for 1 h at 37°C. The optical density (OD) value was measured at 450 nm. The OD value was measured after 24, 48, 72 and 96 h upon treatments, respectively. The experiment was independently repeated three times.

RNA substrates preparation

The rDNA templates for *in vitro* transcription of RNA substrates containing an N-terminal T7 promoter (47S pre-rRNA-4772-5608, 47S pre-rRNA-4772-6099, 47S pre-rRNA-5184-6099) (Supplementary Table S3) were respectively constructed into pcDNA3.1 (+) vector (T7 promoter mutation) after NheI/EcoRV digestion. The rRNA substrates were synthesized *in vitro* by T7 RNA polymerase transcription of the pcDNA3.1(+)-rDNA plasmid linearized with EcoRV, respectively. The transcribed rRNA substrates were extracted from the reaction mixture by 6% Urea-PAGE gel and then stained by SYBR Gold (Thermo Fisher, USA). The rRNA substrates were recovered and stored at -80°C.

The 5′-Cyanine 3 (Cy3)-labeled-rRNA (47S pre-rRNA-5574-5608), 5′-Cy3-labeled-non-rRNA and 5′- Cy3-labeled-rDNA were synthesized by Genescript, China. The sequences of the substrates as follows: 5′-Cy3-rRNA: CGCUUCCCUCCGCACACCCACCCCCCCACCGCGAC; 5′-Cy3-non-rRNA: ACUUUAAGAAGGAGAUAUACCAUG GGCAGCAGCCA; 5′-Cy3-rDNA: CGCTTCCCTCCGCA CACCCACCCCCCCACCGCGAC.

In vitro exonuclease assays

The ISG20L2 exonuclease reaction was carried out in a final volume of 10 μl consisting of 25 mM Tris-HCl pH 7.5, 5 mM $MgCl_2$, 1 mM dithiothreitol (DTT), and 100 μg/ml BSA. The RNA substrates and ISG20L2 wild-type or mutant proteins were added as indicated in the figure legends. The reaction mixtures were incubated at 37°C for the time indicated and quenched by adding 2 × TBE-urea sample buffer (C506046, Sangon Biotech, China). The reaction mixtures were analyzed with 6% (for transcribed RNA substrates) or 12% urea-PAGE gel (for 5′-Cy3-labeled RNA or DNA substrates). For the kinetic analysis, the 5′-Cy3-labeled-rRNA or non-rRNA at concentrations that varied between 20 nM and 1000 nM and ISG20L2 proteins (0.1 ng) were used to determine K_M and k_{cat} values. The gels were visualized using ChemiDoc™ MP Imaging System (Bio-Rad, CA, USA) and quantified using ImageJ software. The amount of RNA substrate degradation in the reaction was determined by calculating the top band reduction in the urea-PAGE gel within the indicated time. To detect the effect of metal ions in the enzymatic activity of ISG20L2, the respective divalent metals, including $MnCl_2$ (0-25 mM), $MgCl_2$ (0-25 mM), $CoCl_2$ (0-25 mM), $CaCl_2$ (0-25 mM) and $ZnCl_2$ (0-25 mM), were added into the reaction mixtures.

Protein expression and purification

The DNA sequence encoding the full length human ISG20L2 (residues 1-353) was synthesized with codon optimization (Genscript, China), and was used as the template for the construction of all mutations. Human ISG20L2 with mutation D327A and N-terminal truncation (Δ1-159) ($ISG20L2^{nuc}$) was amplified and subcloned into the modified pET-15b, which contains an N-terminal hexa-histidine tag and a human rhinovirus (HRV) 3C protease cleavage site.

Escherichia coli BL21 (DE3) containing the $ISG20L2^{nuc}$-pET15b was grown in LB broth media at 37°C to OD_{600} of 0.6-0.8. Then 0.12 mM IPTG was added to induce recombinant protein expression at 16°C for 12 h. Cells were harvested by centrifugation and resuspended in ice-cold lysis buffer (20 mM MES pH 6.0, 500 mM NaCl). The cells were lysed by sonication, and then centrifuged at 30 000 g for 40 min. The supernatant containing the soluble $ISG20L2^{nuc}$ recombinant protein was loaded on a Ni-chelating Sepharose column (GE Healthcare) which was pre-equilibrated by lysis buffer. After washing with buffer (20 mM MES pH 6.0, 500 mM NaCl, 20 mM imidazole), ISG20L2 was eluted using elution buffer (20 mM MES pH 6.0, 200 mM NaCl, 250 mM imidazole). The N-terminal hexa-histidine tag was cleaved by HRV 3C protease. Then the $ISG20L2^{nuc}$ protein was further purified by a 5 ml HiTrap SP HP column (GE Healthcare) and eluted with a 150 ml linear gradient of 0.2-0.6 M NaCl in 20 mM MES pH 6.0 buffer. Finally, the protein $ISG20L2^{nuc}$ was purified using a HiLoad 16/600 Superdex 75 pg column (GE Healthcare) equilibrated with the buffer containing 20 mM MES pH 6.0 and 200 mM NaCl. The purified $ISG20L2^{nuc}$ protein was concentrated to 10 mg/ml.

Crystallization and data collection

Preliminary crystallization was carried out by using the sitting-drop vapor-diffusion method at 18°C by mixing equal volumes of protein $ISG20L2^{nuc}$ and reservoir solution. After optimization, the best crystals of $ISG20L2^{nuc}$ were obtained in a reservoir solution consisting of 0.1 M BIS-TRIS propane pH 9.0, 30% PEG 6000 and 3% v/v 2-Propanol. The $ISG20L2^{nuc}$ crystals were soaked in the cryoprotectant buffer containing the reservoir solution added with 20% (v/v) glycerol, and then flash-cooled in liquid nitrogen. The X-ray data was collected on Beamline BL19U1 at Shanghai Synchrotron Radiation facility (SSRF). The data was processed using HKL-3000 software suite (28). The crystal of $ISG20L2^{nuc}$ belongs to space group P 2_1 2_1 2_1 with the unit cell dimensions $a = 59.0$ Å, $b = 59.0$ Å, $c = 111.3$ Å, and $\beta = 90.00°$.

Table 1. Data collection and refinement statistics of the ISG20L2

	ISG20L2
Data collection[a]	
Space group	P 2_1 2_1 2_1
Cell dimensions	
a, *b*, *c* (Å)	59.0, 59.0, 111.3
α, β, γ	90.0, 90.0, 90.0
Resolution (Å)	52.14–2.77 (2.85–2.77)[b]
R_{merge}	0.064 (0.145)
R_{meas}	0.080 (0.183)
I / σI	11.21 (5.34)
CC(1/2)	0.992 (0.957)
Completeness (%)	92.4 (89.6)
Redundancy	4.1 (4.2)
Refinement	
Resolution (Å)	2.77
No. reflections	17 433
R_{work}/R_{free} (%)	25.0/26.4
No. atoms	
Protein	2552
Water	24
Ligand/Zn	/
B-factors (Å^2)	
Protein	69.6
Water	50.9
Ligand/Zn	/
R.m.s. deviations	
Bond lengths (Å)	0.003
Bond angles (°)	0.680
Ramachandran stat.(%)	93.6 / 6.4 / 0.0[c]

[a]One crystal was used for data collection.
[b]Values in parentheses are for the highest-resolution shell.
[c]Values are in percentage and are for most favored, additionally allowed, and outliers regions in Ramachandran plots, respectively.

Structure determination and refinement

The crystal structure of ISG20L2^{nuc} was solved through molecular replacement by using Phaser program from CCP4 software suite (29). The structure of ISG20 (PDB code: 1WLJ) was used as the search model. The ISG20L2 structure building was performed using the ARP/wARP software (30). Both PHENIX (31) and COOT (32) were further used for manual model building and refinement. All data collection and structure refinement statistics are summarized in Table 1. All the molecular graphics figures are prepared using PyMol (http://www.pymol.org).

Thermal shift assay

To perform the thermal shift assays, 5 ul of fresh 200 × SYPRO orange dye (Thermo Fisher, USA) solution was mixed with 45 μl of 5 μM recombinant proteins in the MES buffer (50 mM MES pH 6.0 and 150 mM NaCl). The thermal melting curves were measured using a Real-Time PCR System (BIO-RAD, CFX96) through a melt curve program with a temperature range from 25°C to 95°C and a ramp rate of 1°C/min. A mixture solution only containing the SYPRO orange dye or the MES buffer was used as the control sample.

Colony formation assay

One thousand cells were plated into 6-well plates with 2 ml complete DMEM medium per well. Then the cells were cultured in a 5% CO_2 humidified incubator at 37°C for 2 weeks. The colonies were fixed with 4% paraformaldehyde for 30 min and stained with Giemsa for 30 min. Finally, the colonies that were >50 cells were counted.

Statistical analysis

Statistical analysis was performed with GraphPad Prism 7.0 software. The data were presented as means ± standard deviation (SD). Statistical significance was analyzed by Student's two-tailed *t*-test, and P value < 0.05 was considered statistically significant.

Results

Human ISG20L2 participates in the ITS1 cleavage of 18S pre-rRNAs

It has been reported that ISG20L2 is involved in the maturation of 5.8S rRNA through the cleavage of the ITS2 region in 12S pre-rRNA (17). To validate the functional role of ISG20L2 in human cells, we generated two ISG20L2 knockout (KO) HEK-293T cell lines using the CRISPR/Cas9 system (Supplementary Figure S1A), and both cell lines exhibited classical HEK-293T cell morphology. The ISG20L2-KO1 cell line was selected for the following experiments.

We used NETN100 buffer to lyse cells and separately extracted RNAs from the NETN100 soluble and pellet fractions. To validate whether the NETN100 soluble and pellet fractions, respectively, correspond to the nuclear and cytoplasmic fractions of cells, we carried out Northern blot assays using probes against U6 small nuclear RNA (U6 snRNA) and cytoplasmic tRNA^{Lys} (ct-tRNA^{Lys}), respectively. Our results showed that U6 snRNA is only detected in the NETN100 pellets, whereas ct-tRNA^{Lys} is exclusively detected in the soluble fraction (Supplementary Figure S1B and C), indicating that the NETN100 pellets and soluble fraction, respectively, represent nuclear and cytoplasmic fractions of cells. Therefore, the RNAs that were extracted from the NETN100 soluble and pellet fractions correspond to cytoplasmic RNA and nuclear RNA, respectively.

Next, we monitored the levels of pre-rRNA intermediates in ISG20L2-KO1 cells using Northern blot with a series of specific probes (Figure 1A). We found that all of the pre-rRNAs we detected were only present in the NETN100 pellet fraction, with the exception of 18S-E pre-rRNA, which can be transported from the nucleus to the cytoplasm (Figure 1B and Supplementary Figure S1D). Thus, we used the RNA extracted from the NETN100 pellets to analyze the pre-rRNAs processing, except for 18S-E pre-rRNA, in ISG20L2-KO1 cells in the following experiments. Additionally, the 18S-E pre-rRNA processing was examined using RNAs that were extracted from both the NETN100 pellet and soluble fractions, respectively. Consistent with the previous report (17), we indeed observed that the depletion of ISG20L2 resulted in an abnormal accumulation of 12S pre-rRNA, the precursor of 5.8S rRNA. Meanwhile, we also observed a slight accumulation of 32S pre-rRNA (Supplementary Figure S1D). Unexpectedly, we found that the depletion of ISG20L2 in HEK-293T cells caused the significant accumulation of 30S, 21S, and 18S-E pre-rRNA fragments, the precursors of 18S rRNA generated after cleavage at site 2 or E(2a) respectively (1), compared to control cells (Figure 1B), and re-expression of ISG20L2 in ISG20L2-depleted cells largely rescued this phenotype (Figure 1B and Supplementary Figure S1B), suggesting that ISG20L2 is able to progress through the ITS1 regions of 30S, 21S and 18S-E pre-rRNAs. Together, our results reveal the difunctional role of ISG20L2 in human ribosomal biogenesis, acting catalytically in both ITS1 and ITS2 processing.

To directly demonstrate the functional relationship between ISG20L2 and other ITS1 processing factors, we individually knocked down the ITS1 removal factors, namely PARN, NOB1 and DIS3, in ISG20L2-KO HEK-293T cells and measured the pre-rRNA intermediates using Northern blot. Consistent with previous results, knockdown of PARN, a nuclear ribosome biogenesis factor involved in the maturation of human 18S rRNA, resulted in a remarkable accumulation of the 18S-E precursors while not affecting other precursors (Supplementary Figure S2A and D) (13,33). Co-depletion of PARN and ISG20L2 amplified this phenotype, leading to a higher accumulation of 18S-E precursors in both the nucleus and cytoplasm. However, the co-depletion of PARN with ISG20L2 did not alter the accumulation of 21S and 30S precursors compared to the sole depletion of ISG20L2. These findings indicate that both ISG20L2 and PARN are involved in the 18S-E precursor trimming, meanwhile ISG20L2 also participates in the processing of other 18S rRNA precursors generated after cleavage at site 2. However, the more detailed processing mechanism needs to be further explored.

We then examined the functional relationship between ISG20L2 and NOB1, an endonuclease that contributed to the final cleavage of 18S-E precursors at site 3 in the cytosol (6,12,14). Northern blot analysis revealed that knockdown of NOB1 resulted in an increased accumulation of 18S-E precursors in cytoplasm but not in the nucleus (Supplementary Figure S2B and D). However, ISG20L2 depletion led to a marked accumulation of 18S-E precursors in both the nucleus and cytoplasm compared to control cells. Co-depletion of ISG20L2 and NOB1 resulted in a significantly higher accumulation of 18S-E precursors in the cytoplasm compared to either single depletion. These results suggest that 18S-E pre-rRNA was trimmed by ISG20L2 in the nucleus, upstream of NOB1 in the cytoplasm. Collectively, these results support the notion that ISG20L2 is a novel enzymatic member involved in 18S pre-rRNA maturation in the nucleus, particularly in the early steps of ITS1 trimming following site 2 cleavage.

Furthermore, we examined the functional relationship between ISG20L2 and DIS3, an essential catalytic subunit of the exosome complex involved in the exonucleolytic maturation of pre-rRNA (6,12,34). Consistent with previous findings, DIS3 knockdown modestly affected the global level of 18S pre-rRNAs. In contrast, we observed an increased accumulation of 12S pre-rRNA, confirming the role of DIS3 in the 5.8S maturation (Supplementary Figure S2C and D) (12,34). Co-depletion of ISG20L2 and DIS3 further enhanced the accumulation of 12S pre-rRNA (Supplementary Figure S2C and D). These results suggest that ISG20L2 functions together with DIS3 in the maturation of 5.8S rRNA.

To further confirm the functional significance of ISG20L2 in ribosomal biogenesis *in vivo*, we examined the ribosome profiles from different cell lines. Compared to control cells, the ISG20L2-KO cells represented increased ratios of 40S and 60S precursors and decreased ratios of 80S monosome and polyribosomes. These imbalanced ribosome profiles were restored by the re-expression of ISG20L2 in ISG20L2-KO cells (Figure 1C). The data reveals that ISG20L2 is a ribosome biogenesis factor that contributes to 18S and 5.8S pre-rRNA processing.

The human ribosome biogenesis is tightly associated with cellular growth rate (6,35), thus we set out to monitor whether ISG20L2 participates in both cell cycle and cell proliferation. It is shown that the ISG20L2-KO cells have an increased fraction of G2/M-phase cells, as well as a reduced fraction of S-phase cells, when compared with those in control cells (Figure 1D and Supplementary Figure S3), indicating that ISG20L2 plays a role in cell cycle transition, which could further affect cell proliferation. Indeed, the depletion of ISG20L2 significantly inhibited cell proliferation relative to control cells (Figure 1E). To verify that the observed cell cycle arrest and impaired cell proliferation were provoked by the ISG20L2 deficiency, we re-expressed ISG20L2 in these ISG20L2-KO cells, and found that the restoring ISG20L2 expression eliminated the abnormal cell cycle arrest in G2/M-phase and restored the fraction of S-phase cells (Figure 1D and Supplementary Figure S3). And the rescued ISG20L2 also restored cell proliferation (Figure 1E). These results revealed that ISG20L2 is involved in both cell cycle transition and cell proliferation.

Catalytic properties of human ISG20L2

To directly characterize the exonuclease activity of recombinant human ISG20L2 *in vitro*, the recombinant ISG20L2 full-length protein, purified from the ISG20L2-overexpressed HEK-293T stable cell line, was incubated with an 837-nt single-stranded RNA (ssRNA) transcript (termed 18S-E segment, 4772-5608 nt in the 47S pre-rRNA) and a synthetic 35-nt ssRNA substrate (5574-5608 nt in the 47S pre-rRNA), respectively. Both the two highly GC-rich ITS1 segments are gradually trimmed by the recombinant wild-type ISG20L2 protein (Figure 2A and Supplementary Figure S4A–C). And ISG20L2 can also digest other highly GC-rich ssRNA transcripts containing different ITS1 regions (Supplementary Figure S4D), confirming the catalytic activity of ISG20L2 towards diverse ITS1 segments. These enzymatic assays also suggest that ISG20L2 is a non-specific exonuclease. Furthermore, we carried out the enzymatic assays of the recombinant ISG20L2 protein with another 35-nt synthetic oligoribonucleotide, which consists of non-rRNA sequence (termed as non-rRNA substrate), and we found that ISG20L2 was also able to digest the non-rRNA substrate, while the 35-nt non-rRNA substrate was digested at a slower rate compared to the 35-nt rRNA substrate (Figure 2B). In contrast, ISG20L2 was unable to digest single-stranded DNA (ssDNA) (Supplementary Figure S4E). In all, our results revealed that ISG20L2 is a non-sequence-specific exoribonuclease, which is consistent with the enzymatic characteristics of ISG20 as a non-sequence-specific exonuclease (16). While these observations provide initial insights into the catalytic specificity of ISG20L2, further experiments are necessary to fully demonstrate its substrate specificity.

A steady-state kinetic analysis, using the 35-nt synthetic ssRNA substrate with various concentrations, was carried out to precisely measure the catalytic constants of ISG20L2. The k_{cat} value for ISG20L2 is 25.6 ± 0.3 s^{-1}, indicating a high turnover number. And the K_M value is 66.4 ± 2.5 nM for the 35-nt synthetic ssRNA, indicating a high binding affinity for the ssRNA substrate (Figure 2C). Additionally, the steady-state kinetic analysis also revealed that ISG20L2 has a higher catalytic efficiency toward rRNA substrate than non-rRNA substrate in the conditions tested (Figure 2C), which is in good agreement with *in vitro* degradation assays (Figure 2B).

To reveal the influence of metal ions on the ISG20L2 exonuclease activity, several different divalent cations (Mg^{2+}, Mn^{2+}, Co^{2+}, Zn^{2+} and Ca^{2+}) were used to measure the catalytic

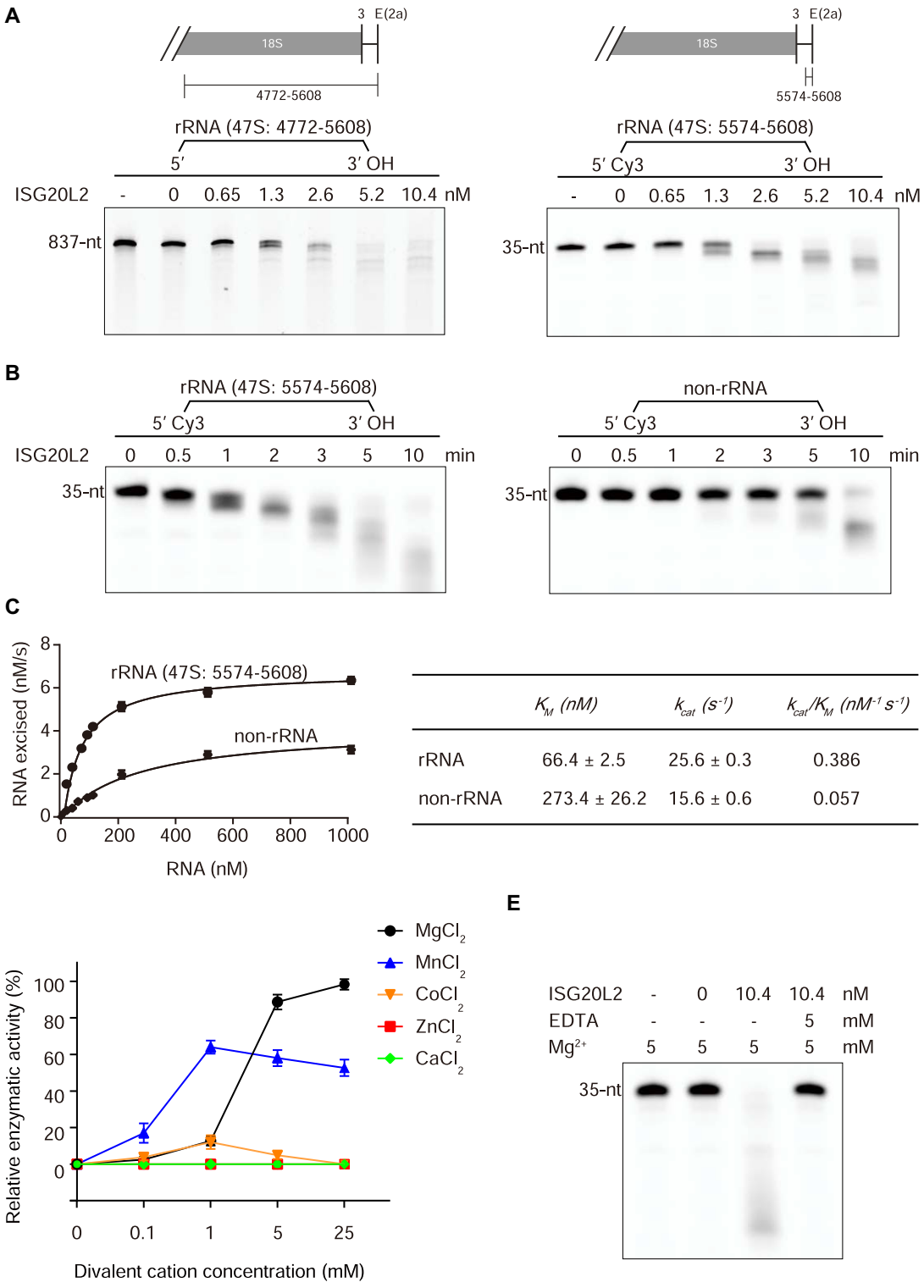

	K_M (nM)	k_{cat} (s^{-1})	k_{cat}/K_M ($nM^{-1}\,s^{-1}$)
rRNA	66.4 ± 2.5	25.6 ± 0.3	0.386
non-rRNA	273.4 ± 26.2	15.6 ± 0.6	0.057

Figure 2. Catalytic properties of ISG20L2. (**A**) The fragment of 47S-rRNA-4772-5608 (containing the 3′ distal position of site E, 837-nt) was transcribed *in vitro* and used for ISG20L2 exonuclease assay. The transcript rRNA substrate was denatured at 90°C and renatured by ramping down for 0.1°C/s to 25°C, and then about 20 nM rRNA was incubated with the recombinant ISG20L2 full-length protein at the indicated concentration for 10 min at 37°C. The reaction mixtures were resolved on 10-well 6% urea-PAGE gel and stained by SYBR Gold (Thermo Fisher). The synthesized 5′-Cy3-rRNA-5574-5608 rRNA substrate (500 nM) was incubated with the recombinant ISG20L2 full-length protein at the indicated concentration for 3 min at 37°C. The reaction mixtures were analyzed on 10-well 12% Urea-PAGE gel. The RNA substrates were schematized on the top. (**B**) Exonuclease assay of the ISG20L2 full-length protein (2.6 nM) using two different RNA substrates (500 nM) and resolved on 15-well 12% urea-PAGE gel. (**C**) Steady-state kinetic analysis of the exonuclease activity of the ISG20L2 protein. Exonuclease reactions (10 μl) were prepared and analyzed, containing ISG20L2 full-length protein (0.1 ng, 0.26 nM) and RNA substrates ranging from 20 to 1000 nM. Incubations were 0 to 3 min at 37°C. (**D**) Reaction requirements of divalent cation for ISG20L2. Reactions were prepared using 2.6 nM ISG20L2 full-length protein and the indicated reaction modification was plotted. (**E**) The exonuclease activity of ISG20L2 was inhibited in the presence of 5 mM EDTA. The synthesized 5′-Cy3-rRNA-5574-5608 rRNA substrate (500 nM) was used in this assay.

efficiencies of ISG20L2. It is shown that ISG20L2 prefers Mg^{2+} with maximum activity detected at or more than the concentration of 5 mM. ISG20L2 can also use Mn^{2+} with decreased activity detected in a wider effective concentration. The addition of Co^{2+} resulted in a significant decrease in the ISG20L2 activity, retaining almost 6% as compared to that in the presence of Mg^{2+}. ISG20L2 cannot utilize Zn^{2+} and Ca^{2+} for catalysis (Figure 2D). It suggests that ISG20L2 can digest ssRNA substrate in the presence of Mg^{2+} under a concentration-dependent manner. While the enzymatic activity of ISG20L2 was inhibited in the presence of 5 mM ethylene diamine tetra-acetic acid (EDTA) (Figure 2E), indicating that the Mg^{2+} plays an essential role in the activity of ISG20L2.

Overall structure of human ISG20L2 exonuclease domain

To provide structural insights into the molecular mechanism of ISG20L2 for the processing of pre-rRNAs, we carried out crystallographic studies and obtained crystals of human ISG20L2 nuclease domain ($ISG20L2^{nuc}$, residues 160-353) with the D327A mutation, since our attempts to purify $ISG20L2^{nuc}$ wild-type protein were unsuccessful. The thermal shift assay revealed that the D327A mutant has a very similar melting temperature with the wild-type ISG20L2 (Supplementary Figure S5), indicating that this mutation does not affect the overall folding of ISG20L2, thus the structure of $ISG20L2^{nuc}$ with the D327A mutation is used to represent the three-dimensional conformation of wild-type $ISG20L2^{nuc}$. The crystal structure of $ISG20L2^{nuc}$ was determined at 2.9 Å resolution and refined to a $R_{work} = 25.0\%$ and $R_{free} = 26.4\%$ with good stereochemistry.

The final model contains two protein molecules in the asymmetric unit, named A and B respectively (Figure 3A). The root mean square deviation (RMSD) between $ISG20L2^{nuc}$ molecule A and B is 0.357 Å, indicating that the two $ISG20L2^{nuc}$ molecules in the complex have almost identical structures (Supplementary Figure S6). The $ISG20L2^{nuc}$ molecule A was used for the following structural analysis. The $ISG20L2^{nuc}$ monomer contains a core five-stranded twisted β sheet flanked by α-helices at each side of β sheet (α2, α3 on the one side, and α1, α4, α5 on the opposite side), resembling the common αβα fold of DEDD 3′-5′ exonucleases (Figure 3B). Additionally, a 3_{10}-helix (residues 287-289) is observed in the crystal structure of $ISG20L2^{nuc}$ (Figure 3B). The residues 177-347 from the DEDD domain are clearly observed in the structure, and there is no electron density observed for the N-terminal and C-terminal regions (residues 160-176 and 348-353, respectively). Additionally, no electron density is observed for the residues 290-299 and 318-321 from β5-α4-loop and α4-α5-loop respectively, suggesting the high flexibility of the two loops, both of which appear to play important roles in RNA substrate recognition and binding (see below).

Structural alignment using the DALI server reveals that the closest homologues of $ISG20L2^{nuc}$ are *Homo sapiens* ISG20 (HsISG20, PDB code: 1WLJ, *Z* score of 22.5, RMSD: 1.6 Å), the DEDDh domain of *Arabidopsis thaliana* SDN1 (AtSDN1, PDB code: 5Z9X, Z score of 15.4, RMSD: 1.9 Å) and the catalytic domain of *S. cerevisiae* Pan2 exonuclease (ScPan2, PDB code: 6R9J, *Z* score of 13.4, RMSD: 2.3 Å) (Figure 3C). The DEDD domains from the four proteins are highly conserved not only in amino-acid sequence but also in overall conformation, sharing the common DEDD nuclease fold, an open αβα fold comprising a central β-sheet flanked by α-helices (Figure 3C and D). In addition, the ISG20L2 DEDD domain also shares a similar conformation with other exonucleases in spite of low sequence similarity, such as *H. sapiens* ERI3 (PDB code: 2XRI), *Mus musculus* TREX2 (PDB code: 6A45 and 6A47) and TREX1 (PDB code: 5YWS), and *Caenorhabditis elegans* CRN4 (PDB code: 3CG7).

Structure of the catalytic pocket in ISG20L2

Similar to its homologous proteins, the catalytic pocket of $ISG20L2^{nuc}$ is surface exposed and located in the hollow near the center formed by residues from β1, α4, α5, β3-α1-loop, α4-α5-loop and β5-α4-loop (Figure 4A and Figure 5). Previous studies have reported that DEDDh exonucleases have five fully conserved residues which are crucial for their enzymatic activity (16,36–39). Sequence alignment revealed that the DEDDh motif in ISG20L2 includes Asp^{183}, Glu^{185}, Asp^{267}, His^{322} and Asp^{327}, corresponding to Asp^{11}, Glu^{13}, Asp^{94}, His^{149}, Asp^{154} in HsISG20, and Asp^{144}, Glu^{146}, Asp^{228}, His^{278}, Asp^{283} in AtSDN1, and Asp^{910}, Glu^{912}, Asp^{1020}, His^{1066}, Asp^{1071} in ScPan2 respectively (Figure 3D and Figure 4B).

Given that the Asp^{327} was mutated to Alanine in the crystal structure of $ISG20L2^{nuc}$, to better demonstrate the catalytic role of these conserved acidic residues, this Alanine was *in silico* reversely mutated to aspartic acid by using the PyMol Mutagenesis tool (https://pymolwiki.org/index.php/Mutagenesis), and the optimal conformation of Asp^{327} was selected based on the Ramachandran plot analysis (Supplementary Figure S7). Furthermore, the structural analysis revealed that the optimal conformation of Asp^{327} in the mutation model of ISG20L2 is almost same to that of Asp^{327} in the AlphaFold model of ISG20L2 (Supplementary Figure S8A). Combining these analyses, it suggests that the conformation of Asp^{327} in the mutated model of ISG20L2 is reliable, and can be used for the following structural analysis of the catalytic pocket. Structural superposition shows that the catalytic residues Asp^{183}, Glu^{185}, Asp^{267} and Asp^{327} in ISG20L2 are found at the equivalent positions in the HsISG20, AtSDN1 and ScPAN2 structures (Figure 4B). Given that HsISG20, AtSDN1 and ScPAN2, used in the structural comparison, are in ligand-binding states, it suggests the stable conformation of the four conserved acidic residues in both ligand-free and -bound states. In comparison, the side-chain of the fifth conserved residue His^{322} from α4-α5-loop, is in an outward-facing conformation, facing away from the active pocket (Figure 4B). Meanwhile, no catalytic metal ions are observed in the active site of ISG20L2 according to the electron density (Figure 4B). We have revealed that Mg^{2+} is essential for the enzymatic activity of ISG20L2 (Figure 2E), and structural superposition revealed that the catalytic pocket of ISG20L2 can accommodate two catalytic metal ions (Supplementary Figure S9). And the $ISG20L2^{nuc}$-Mg^{2+} model revealed that catalytic residues Asp^{183}, Glu^{185}, Asp^{267} and Asp^{327} are involved in the binding of the functional Mg^{2+} ions via hydrogen bonds at the active site (Figure 4C). Additionally, the ultimate phosphate moiety is also responsible for the binding of the two functional Mg^{2+} ions (see below). Single point mutation of conserved residues (Asp^{183}, Glu^{185}, Asp^{267}, His^{322} and Asp^{327}) completely abolished the enzymatic activity of ISG20L2 (Figure 4D), revealing that the five catalytic residues are essential for the exonuclease activity of ISG20L2.

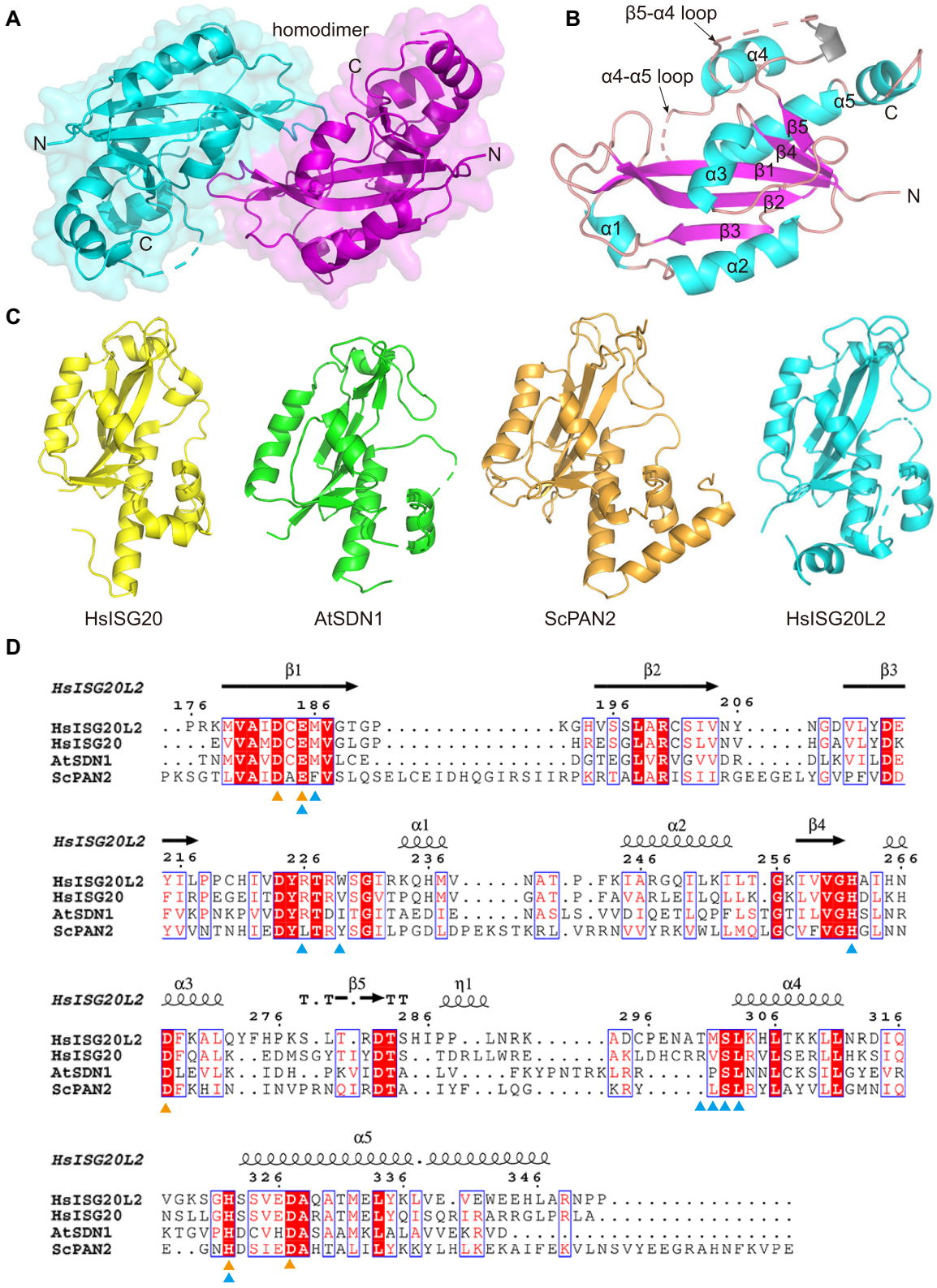

Figure 3. Overall structure of the human ISG20L2^{nuc}. (**A**) ISG20L2^{nuc} exists as a homodimer in the asymmetric unit. One monomer is shown in cyan, and the other is shown in magenta. (**B**) The cartoon representation of ISG20L2^{nuc} monomer. Five α-helices (cyan) and five β-strands (magenta) are labelled. The 3_{10}-helix is in gray. (**C**) Comparison of the similar structural folding of human ISG20L2^{nuc} (HsISG20L2) homologs. From left to right: HsISG20, human ISG20 (PDB code: 1WLJ); AtSDN1, the DEDDh domain of *Arabidopsis* SDN1 (PDB code: 5Z9X); ScPAN2, the catalytic domain of ScPan2 exonuclease (PDB code: 6R9J). (**D**) The primary sequence alignment of ISG20L2 with its homologous proteins. The catalytic residues are displayed in orange triangles. The RNA substrate binding residues are in blue triangles.

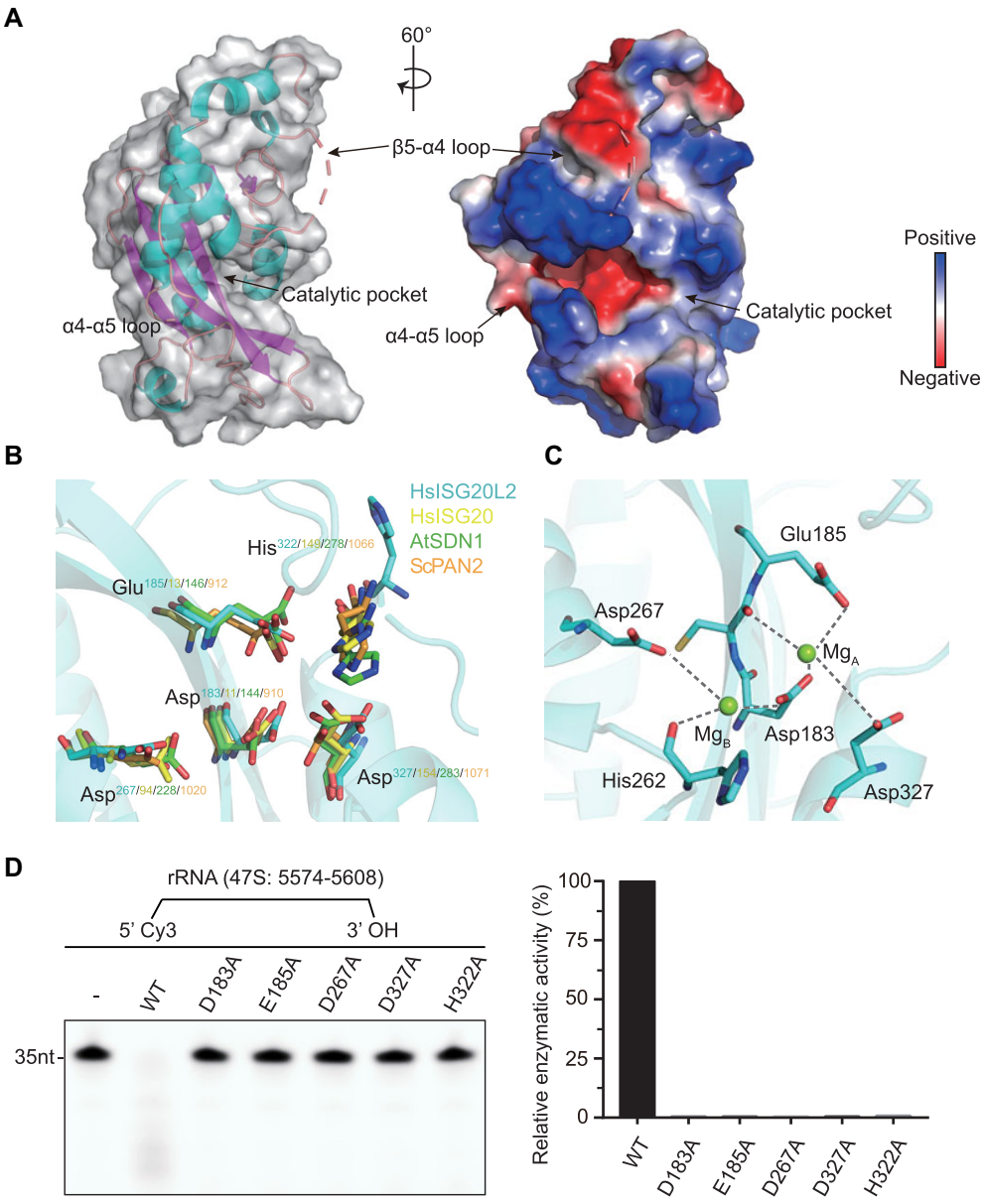

Figure 4. Structural analysis of the active site of human ISG20L2^{nuc}. (**A**) The surface (left) and electronic potential map (right) of ISG20L2^{nuc}. The flexible α4-α5 loop, β5-α4 loop, and catalytic pocket are indicated. (**B**) The catalytic residues in the ISG20L2 are superposed with HsISG20, AtSDN1 and ScPAN2. (**C**) Interaction model between the catalytic residues (cyan sticks) and two Mg^{2+} ions (green spheres) in ISG20L2. The hydrogen bonds are displayed in grey dashes. (**D**) *In vitro* enzymatic assays of wild-type ISG20L2 and the mutants of catalytic residues. The 500 nM synthesized 5′-Cy3-rRNA-5574-5608 rRNA substrate was incubated with 2.6 nM recombinant full-length protein for 3 min at 37°C. WT: wild-type.

The RNA binding mode in human ISG20L2

Structural superposition of ISG20L2 with the closely related nucleases AtSDN1 and ScPan2 respectively, both of which contain ssRNA in the catalytic pocket (PDB code: 5Z9X for AtSDN1, PDB code: 6R9J for ScPan2), revealed how RNA could bind to the conserved catalytic pocket of ISG20L2 (Figure 5A). The model shows good positioning of the ssRNA in the catalytic pocket of ISG20L2. Similar to the two nucleases AtSDN1 and ScPan2, the scissile phosphate bond between the ultimate and penultimate ribonucleotides in the RNA substrate is directly faced to Mg^{2+} ions and the side chains of acidic amino acids from the DEDD motif (Figure 5A, zoomed region), and a hydrogen bond network is formed between Asp^{183}, Glu^{185}, Asp^{267}, Asp^{327}, two Mg^{2+} ions, and the ultimate phosphate moiety. Meanwhile, the side-chain of Glu^{185} forms a hydrogen bond with the 3′-OH group of the ribose in ultimate ribonucleotide (Figure 4C and Figure 5B).

In addition, the ISG20L2-RNA model also revealed several interactions between RNA and residues in the active pocket, including Met^{186} from β1, Arg^{226} from β3-α1-loop, His^{262} from β4-α3-loop, and Thr^{300}, Met^{301}, Ser^{302} and Leu^{303} from β5-α4-loop. These residues are probably engaged in RNA recognition through forming hydrogen bonds with RNA 2′- and 3′-OH groups, as well as phosphate moieties (Figure 5B). Consistent with the homologs AtSDN1 and HsISG20 (16,36), the main-chain of Met^{186} and side-chain of Arg^{226} (corresponding to Met^{147} and Arg^{185} in AtSDN1, Met^{14} and Arg^{53} in HsISG20) are involved in the binding and stabilization of the ultimate ribonucleotide via hydrogen bonds in ISG20L2 (Figure 5B). To further examine the functional importance

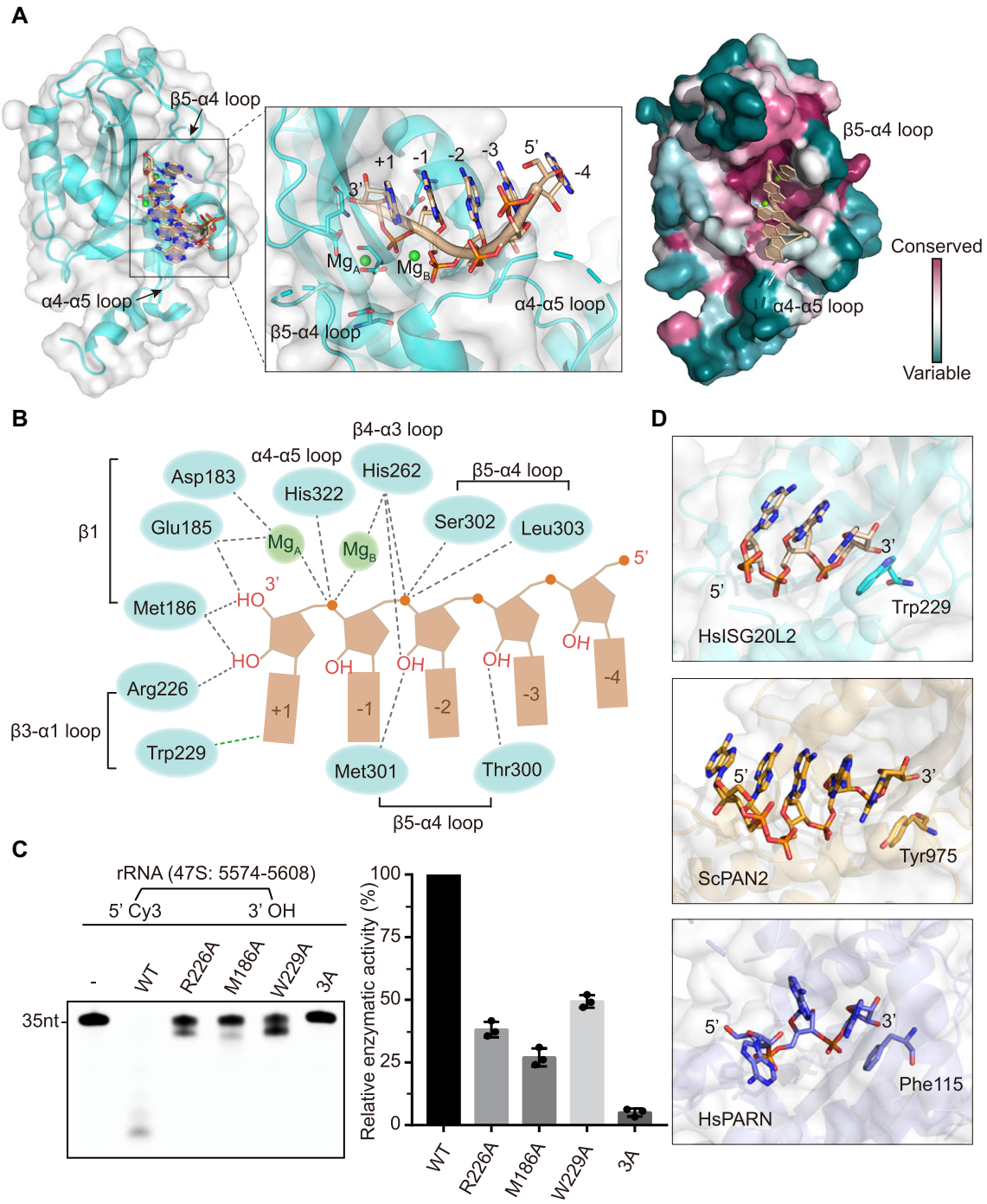

Figure 5. The RNA-ISG20L2^{nuc} interaction mode. (**A**) The RNA and Mg^{2+} ions were placed by superposition with the ScPAN2-oligo(A)$_5$ complex (PDB code: 6R9J). RNA binding residues conservation was mapped onto the surface of ISG20L2^{nuc}. The Mg^{2+} ions and the acidic residues from the DEDDh motif are shown in green spheres and cyan sticks, respectively. (**B**) The schematic drawing of the potential interactions between the RNA substrate and ISG20L2. (**C**) *In vitro* enzymatic assays of ISG20L2 wild-type and the mutants of RNA substrate binding residues. 3A: M186A-R226A-W229A. The 500 nM synthesized 5′-Cy3-rRNA-5574-5608 rRNA substrate was incubated with 2.6 nM recombinant full-length protein for 3 min at 37°C. (**D**) The stacking interaction between RNA and ISG20L2 homologs. From top to bottom: HsISG20L2, ScPAN2 (PDB code: 6R9J) and HsPARN (PDB code: 2A1R).

of Met^{186} and Arg^{226} in the enzymatic activity of ISG20L2, we generated two single-site mutants (M186A, R226A), and measured the enzymatic activities of the ISG20L2 mutants. Compared to ISG20L2 wild-type protein, the enzymatic activities of the mutants Met186A and Arg226A were reduced to 27% and 38%, respectively (Figure 5C), indicating the functional significance of Met^{186} and Arg^{226} in the catalytic reaction of ISG20L2. These RNA binding residues are conserved among DEDD nucleases (Figure 3D and Figure 5A). It suggests that the hydrogen-bonding networks between the RNA sugar-phosphate backbone and protein are commonly conserved in the DEDDh nucleases (36).

Another potentially important residue identified in the ISG20L2-RNA model is Trp^{229} from β3-α1-loop, which exists at the bottom of the active site and is close to the ultimate base of the RNA substrate. It suggests that the aromatic

ring of Trp^{229} forms a π-stacking interaction with the ultimate base of the RNA substrate (Figure 5D). The Trp^{229} in ISG20L2 is structurally conserved in ScPan2 and *Homo sapiens* PARN (HsPARN), equivalent to Tyr^{975} and Phe^{115} in ScPan2 (PDB code: 6R9J) and HsPARN (PDB code: 2A1R) respectively, forming π-stacking interactions with the 3′ terminal base of RNA (Figure 5D), which are important for their enzymatic activities (37,40,41). Similarly, the enzymatic activity of the mutant W229A was reduced to 49%, indicating the functional importance of Trp^{229} in the catalytic activity of ISG20L2. Furthermore, the triple mutant M186A-R226A-W229A almost fully abolished the enzymatic activity (Figure 5C). The mutagenesis assay highlighted the functional importance of the Met^{186}, Arg^{226} and Trp^{229} in the binding of RNA substrate and all three residues are involved in 3′ tail nucleotide binding to position the RNA substrate at a precise orientation, facilitating the catalytic reaction of ISG20L2. In comparison, the Trp^{229} in ISG20L2 was replaced by Val^{56} and Ile^{188} in HsISG20 and AtSDN1 respectively (Figure 3D), revealing the RNA substrate binding diversity between ISG20L2 and its homologous proteins.

Together, the ISG20L2-RNA model reveals that the ribose-phosphate backbone mediates virtually all contacts between ISG20L2 and RNA substrate, and no canonical base-specific interactions are observed, suggesting that ISG20L2 is non-sequence-specific exonuclease, which is consistent with our biochemical data (Figure 2B).

The catalytic mechanism of ISG20L2

Structural comparison between ISG20L2^{nuc} apoenzyme with its homologous protein-RNA complexes revealed that the most significant structural variations in the catalytic pocket occurred in the α4-α5-loop of ISG20L2 (corresponding to residues 267-279 and 1056-1068 in AtSDN1 and ScPAN2, respectively) (Figure 6A). In detail, the α4-α5-loop exhibits an outward-open conformation in ISG20L2^{nuc} apoenzyme, and the side-chain of His^{322} from the α4-α5-loop is facing away from the active site, and the adjacent residues 318-321 are in disorder (Figure 4B and Figure 6A). In comparison, the corresponding region in AtSDN1/ScPAN2-RNA complex is in an inward-closed conformation, the corresponding residue His^{278}/His^{1066} in AtSDN1/ScPAN2 orients directly towards the active site, and the side-chain imidazole group is hydrogen bonded to the ultimate phosphate moiety of the RNA substrate (Figure 6A and Supplementary Figure S10). Additionally, in ISG20L2^{nuc} apoenzyme, the average B-factor value for the overall ISG20L2^{nuc} protein molecule is 66.49 Å, while the average B-factor for the α4-α5-loop is 94.35 Å, which is higher than that of its surrounding residues or the whole ISG20L2^{nuc} protein molecule (Figure 6B). And structural superposition between the molecules A and B, existing in the asymmetric unit in the final model of ISG20L2^{nuc}, revealed that, compared to molecule A, the His^{322} and the α4-α5 loop adopt different conformations in molecule B, suggesting the intrinsic flexibility of α4-α5 loop (Supplementary Figure S8B). Thus, these analyses revealed that the α4-α5-loop in ISG20L2 is structurally dynamic in the absence of RNA substrate.

Sequence alignment shows that the amino acid residue corresponding to His^{322} is fully conserved in all ISG20L2 orthologs (Figure 3D), indicating the functional resemblance of the conserved histidine during the catalytic process. Furthermore, the enzymatic catalytic importance of His^{322} in ISG20L2 has been confirmed in our biochemical data that the H322A mutant completely abolished the enzymatic activity of ISG20L2 (Figure 4D). Combining the aforementioned conformational diversity of His^{322} in ISG20L2^{nuc} apoenzyme compared to its homologous protein-RNA complexes (Figure 6A), it suggests that the His^{322} and its surrounding residues from the α4-α5-loop of ISG20L2 undergo a disorder-to-order transition upon RNA substrate binding to ensure the imidazole group of His^{322} forms a hydrogen bond with the ultimate phosphate moiety, facilitating the His^{322} to carry out its catalytic role (Figure 6C). A similar conformational change is observed in the nuclease TREX2, in which the conserved His^{188} (corresponding to His^{322}) is outward to the catalytic site in the apo-state (PDB code: 6A45), while the His^{188} points to the active pocket in the RNA substrate-binding state, forming a hydrogen bond with the scissile phosphate bond of the nucleic acid substrate (PDB code: 6A47 and 6A4B) (42).

Given the full conservation of DEDDh motif and RNA binding orientation, ISG20L2 is likely to adopt the identical catalytic mechanism proposed for DEDD exonucleases (16,39,43), in which the conserved His^{322} functions as the general base to deprotonate the catalytic water molecule (also working as the Mg^{2+}-coordinated water), which thereby carries out nucleophilic attack on the last phosphorus atom for the cleavage of the scissile phosphate bond of the RNA substrate (Figure 6D).

ISG20L2 exonuclease activity is required for colon cancer cell proliferation

Our results above showed the functional importance of ISG20L2 exonuclease activity in ribosome biogenesis and cell growth. We next studied the impact of catalytic residues and RNA binding residues of ISG20L2 *in vivo* using Northern blot. The ISG20L2-KO HEK-293T cells were transfected with ISG20L2 wild-type or the representative ISG20L2 mutant (H322A, M186A-R226A-W229A), respectively. We found that expression of the ISG20L2 mutant H322A or M186A-R226A-W229A in ISG20L2-KO cells failed to reduce the abnormal accumulation of 30S, 21S and 18S-E fragments which are provoked by the ISG20L2 depletion, while restoring the ISG20L2 wild-type expression is able to reduce the accumulation of these precursors (Figure 7A and Supplementary Figure S11B). Meanwhile, the expression of the ISG20L2 mutant H322A or M186A-R226A-W229A cannot reduce the abnormal accumulation of 12S pre-rRNA, while the re-expression of the wild-type ISG20L2 is able to reduce the accumulation of the 12S precursor (Supplementary Figure S11A and B). Together, these data confirmed that both catalytic residues and RNA substrate binding residues of ISG20L2 play essential roles in ribosome biogenesis *in vivo*.

Considering that ribosome biogenesis is tightly associated with cancer progression (2,44–46), we performed bioinformatics analysis using the datasets from the Cancer Genome Atlas (TCGA) and cBioPortal. The pan-cancer analysis revealed that ISG20L2 is aberrantly up-regulated in several cancers, such as breast invasive carcinoma (BRCA), colon adenocarcinoma (COAD), hepatocellular carcinoma (HCC), and lung adenocarcinoma (LUAD), compared to the paired non-cancerous tissues (Supplementary Figure S12), consistent with the previous studies which have suggested the high expression of ISG20L2 in BRCA, HCC and LUAD, and suggested

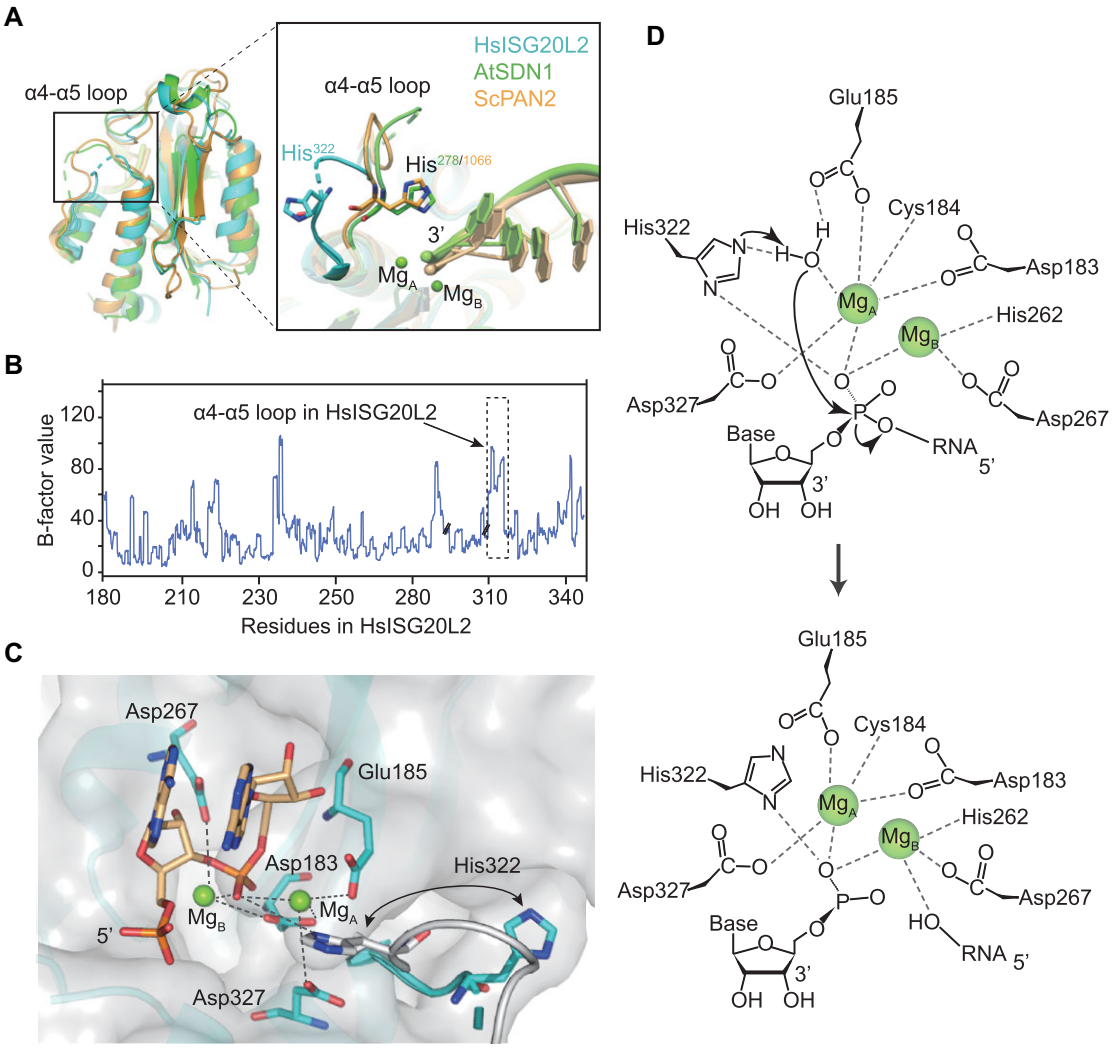

Figure 6. The catalytic mechanism of human ISG20L2. (**A**) Structural comparison between ISG20L2^{nuc} apoenzyme with its homologs bound to RNA, including AtSDN1 (PDB code: 5Z9X) and ScPAN2 (PDB code: 6R9J). The zoomed region reveals the significant structural variations surrounding the catalytic pocket. (**B**) The schematic drawing of the B-factor value of ISG20L2^{nuc}. The α4-α5 loop is indicated. (**C**) The conformational transition of α4-α5 loop upon RNA binding to ISG20L2. The hydrogen bonds formed among catalytic residues, two Mg^{2+} ions and RNA substrate are displayed as grey dashes. (**D**) The proposed enzymatic mechanism of ISG20L2 as exonuclease.

the roles of ISG20L2 as potential diagnostic and prognostic markers (47–49). Nevertheless, there is scant information about the functional role of ISG20L2 in COAD. We first validated the high expression of ISG20L2 in COAD cell lines SW620, HCT116, HT29 and SW480 compared with that in the normal colonic epithelial cell line NCM460 (Figure 7B). Then we used two independent shRNAs to knock down ISG20L2 in SW480 cells (Figure 7C). Based on Western blot results, we selected the shRNA1 for the following experiments (Figure 7C).

It has been well documented that perturbations in ribosome biogenesis can trigger nucleolar stress, which stimulates p53 activation, and finally results in p53-dependent cell cycle arrest or apoptosis (50,51). We suggest that ISG20L2-depletion will lead to an imbalance of ribosome biogenesis and consequent nucleolar stress, which is likely the primary mechanism of cell cycle arrest and proliferation suppression in ISG20L2-depletion cells. To test this, we measured the expression levels of p53 and its targets in human colon cancer SW480 cells and ISG20L2-depletion SW480 cells using Western blot. Our results showed that ISG20L2-depletion promoted the expression levels of p53 and its target p21, meanwhile, the genes CDK1 and CyclinB1, both of which are involved in the G2/M-phase of the cell cycle (52,53), were down-regulated in ISG20L2-depletion cells (Supplementary Figure S13). Therefore, it suggests that ribosome biogenesis imbalance and the consequent nucleolar stress are the major reasons for the cell cycle arrest and proliferation suppression in ISG20L2-depletion cells.

Subsequently, we selected shRNA1 for the following CCK8 and clonogenic assays to explore the potential involvement of ISG20L2 in the tumorigenesis of COAD. The CCK8 assay demonstrated that ISG20L2 KD markedly reduced cell proliferation in SW480 cells (Figure 7D). Consistently, the clonogenic assay showed that ISG20L2 KD significantly decreased the colony formation of SW480 cells (Figure 7E). Notably, the re-expression of wild-type ISG20L2 restored colony-forming capacity and cell proliferation in SW480 cells, whereas the nuclease-deficient ISG20L2 mutants H322A and M186A-R226A-W229A failed to do so (Figure 7D and E,

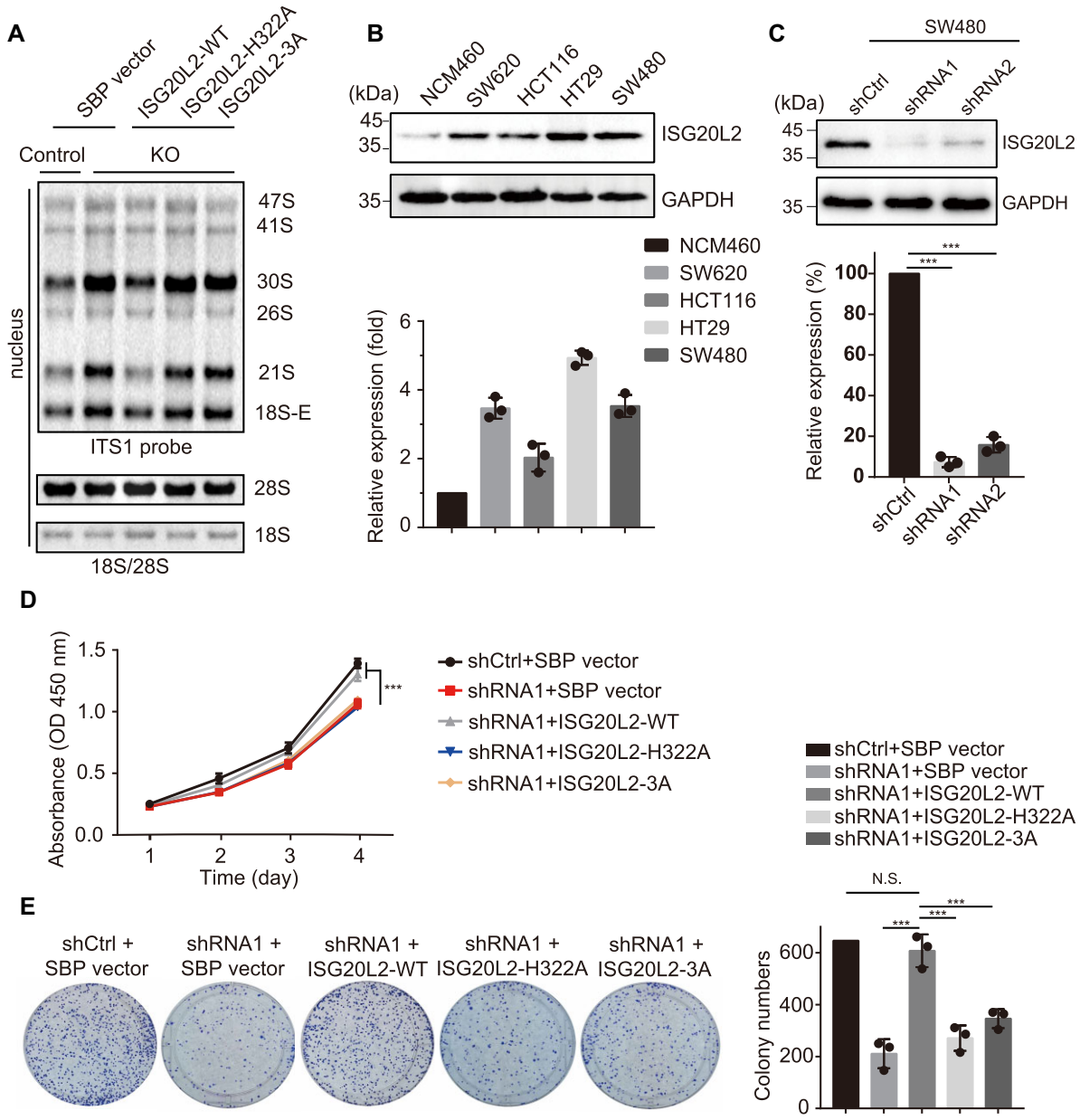

Figure 7. The catalytic activity of ISG20L2 is required for SW480 cell proliferation. (**A**) Expression of nuclease-inactive ISG20L2 mutant H322A or M186A/R226A/W229A failed to rescue the abnormal accumulation of 18S pre-RNA intermediates in ISG20L2-depleted cells. 3A: M186A-R226A-W229A. SBP vector: the modified pIRES2-EGFP vector containing two FLAG-tag, one S-tag and one Streptavidin-Binding Peptide (SBP)-tag. (**B**) Western blot and quantitative analyses of ISG20L2 expression in four colon cancer cell lines and the corresponding normal colonic epithelial cell line NCM460. GAPDH was used as the loading control. Histograms representing quantifications of ISG20L2 levels over GAPDH ($n = 3$) are shown at the bottom. (**C**) Validation of ISG20L2 stable knockdown (KD) cell lines. SW480 cells were transfected with shRNA1, shRNA2 or shCtrl, respectively. The ISG20L2-KD SW480 cells were examined by Western blot. GAPDH was used as the loading control. Histograms represent the quantifications of ISG20L2 levels over GAPDH. Mean ± SD, $n = 3$. ***, $P < 0.001$. (**D**) Cell proliferation of control, ISG20L2-KD, ISG20L2-KD-WT, ISG20L2-KD-H322A and ISG20L2-KD-3A SW480 cells. Mean ± SD, $n = 3$. ***, $P < 0.001$. 3A: M186A-R226A-W229A. (**E**) Colony formation assays of control, ISG20L2-KD, ISG20L2-KD-WT, ISG20L2-KD-H322A and ISG20L2-KD-3A SW480 cells. Mean ± SD, $n = 3$. ***, $P < 0.001$; N.S., no significance. WT: wild-type, 3A: M186A-R226A-W229A.

and Supplementary Figure S14). These results revealed that ISG20L2 exonuclease activity promotes colon cancer cell survival and growth.

Discussion

Although considerable progress has been made in human ribosome biogenesis, the ribonucleases involved in the processing of diverse pre-rRNA intermediates have not yet been fully identified until now. It has been reported that human exonuclease ISG20L2 is responsible for the ITS2 processing, specifically for 12S pre-RNA processing (17). Given that human ISG20L2 is homologous to yeast Rex4, which is involved in yeast ITS1 processing and ribosome biogenesis (18), we performed experiments to reveal whether ISG20L2 is involved in human ITS1 processing. Notably, we found that the ISG20L2 KO in HEK-293T cells caused significant accumulation of 30S, 21S, and 18S-E pre-rRNA fragments, and

re-expression of ISG20L2 is able to rescue this phenotype, suggesting the functional role of ISG20L2 in the ITS1 processing. Meanwhile, we also observed that ISG20L2 is involved in ITS2 processing, consistent with the previous study (Supplementary Figure S1D) (17). These data revealed the dual function of ISG20L2 in human ribosome biogenesis, participating in both ITS1 and ITS2 processing. Indeed, polyribosome profile analysis showed that ISG20L2 contributes to ribosomal biogenesis *in vivo*, also revealing the significance of ISG20L2 in human ribosome biogenesis.

We explored the functional relationship between ISG20L2 and the ITS1 processing factors PARN and NOB1. In contrast to PARN, which solely handles the trimming of 18S-E precursors, ISG20L2 is engaged in the processing of other 18S rRNA precursor species generated following cleavage at site 2, in addition to 18S-E precursors. It appears that ISG20L2 functions independently of PARN and processes 18S rRNA precursors before PARN does. As for the functional relationship between ISG20L2 and NOB1, our data indicates that ISG20L2 acts upstream of NOB1. Additionally, we found that ISG20L2 works together with DIS3 in the ITS2 processing. Collectively, these data revealed the functional redundancy of human ribonucleases in ribosome biogenesis, which is important to preserve rRNA processing in the case of one of them being absent.

Our results showed the functional importance of ISG20L2 exonuclease activity in human ribosome biogenesis and cell growth, and then provided structural insights into the molecular mechanism of ISG20L2 underlying pre-rRNA processing. The ISG20L2^{nuc} shares the common αβα fold of the DEDDh family members. The active pocket represents conformational flexibility in the absence of RNA substrate, and the α4-α5-loop undergoes a disorder-to-order transition upon RNA substrate binding to ensure the His^{322} orients directly toward the active site and carries out its catalytic role. The high similarity of the active site of ISG20L2 with those of DEDDh family members suggests that these DEDDh family members adopt a common catalytic mechanism (Figure 6D).

In addition to the catalytic roles described above about the DEDDh motif in the enzymatic activity of ISG20L2, we noticed that an extensive hydrogen bond network is formed among the Asp^{183}, Glu^{185}, Asp^{267}, Asp^{327} and His^{322} from the DEDDh motif, Mg^{2+} ions and the ultimate ribonucleotide (Figure 5B and Figure 6C), suggesting the mutual stabilizing interactions among the DEDDh motif, functional metal ions, and RNA substrate. The four acidic residues (DEDD), Mg^{2+} ions, and His^{322}, almost located at each side of the scissile phosphate bond respectively, function together as a clamp to hold the ultimate phosphate moiety of the RNA substrate in a precise orientation, facilitating the catalytic reaction of ISG20L2 (Figure 5B and Figure 6C). In turn, the RNA substrate binding can assist in the stabilization of His^{322} and its adjacent residues from the α4-α5-loop in ISG20L2. Given that the RNA-binding pattern in ISG20L2 is similar to that of its orthologs AtSDN1 and ScPan2, it suggests that the mutual stabilizing interactions among the DEDDh motif, functional metal ions and RNA substrate are evolutionarily conserved characteristics for DEDDh nuclease family members.

Ribosome biogenesis plays an important role in cancer progression (4,46,54). In many cancers, ribosome biogenesis and protein synthesis are significantly enhanced to sustain cancer cells growth and proliferation (4,44). And a typical cancer cell can synthesize at least 10 000 different proteins (4,55). Additionally, the free ribosome proteins can modulate many cellular processes including DNA repair, cell cycle, cell proliferation, apoptosis, cell migration, and invasion, all of which are tightly associated with tumorigenesis (2,45,46), revealing the significance of ribosome protein in cancer development. Together, ribosome biogenesis and ribosome proteins could work as attractive anti-cancer targets (2,4). And several reports have suggested that human ISG20L2 is associated with BRCA, HCC and LUAD, and may work as new biomarkers in these cancers (47–49). In this paper, the bioinformatics analysis showed that human ISG20L2 is aberrantly up-regulated in COAD compared to the paired noncancerous tissue. And we first revealed that ISG20L2 exonuclease activity is required for colon cancer cell proliferation. Given that ISG20L2 is involved in ribosome biogenesis in human cells, and that the exonuclease-dependent catalytic residues and RNA substrate binding residues of ISG20L2 are essential for ribosome biogenesis *in vivo*, we hypothesize that the mechanism of ISG20L2 on cancer cell proliferation may be associated with its functional role in human ribosome biogenesis. The up-regulation of ISG20L2 in colon cancer cell is beneficial for the increased production of ribosome, which subsequently facilitates protein synthesis, finally meeting the enhanced protein need for proliferating cancer cells.

We showed the cell cycle arrest and proliferation suppression in ISG20L2-depletion cells and revealed that this phenomenon is attributed to the nucleolar stress triggered by the pre-rRNA processing defects due to ISG20L2 depletion, which promotes p53 activation and consequently leads to p53-dependent cell cycle arrest or apoptosis. Indeed, compared to control cells, ISG20L2-KO cells have an increased fraction of G2/M-phase cells as well as a reduced fraction of S-phase cells. However, no accumulation of G1-phase cells is observed in ISG20L2-KO cells, which is unexpected given the established function of p53 in regulating both the G1/S and G2/M transitions (56–58). Meanwhile, it has also been reported that p53 up-regulation only induces G2/M cell cycle arrest (59). One possible explanation for the absence of G1-phase accumulation in ISG20L2-KO cells is that the p53-dependent cell cycle arrest at the G1/S transition is not triggered by the nucleolar stress response alone, but also requires additional signals such as DNA damage, ribonucleotide depletion, or abnormal proliferative signals (60–63). Further experiments are needed to elucidate the molecular mechanisms underlying the differential response of ISG20L2-KO cells to nucleolar stress at different phases of the cell cycle.

In summary, our results reveal that ISG20L2 is a novel enzymatic member for the 18S pre-rRNA maturation through processing the ITS1 region in the nucleus, provide structural and biochemical insights into the molecular mechanism of ISG20L2 underlying pre-rRNA trimming, and finally suggest that ISG20L2 is a potential therapeutic target for colon adenocarcinoma in future.

Data availability

The atomic coordinate and structure factor for the human ISG20L2 have been deposited in the Protein Data Bank under the Accession Code 7YW5.

Supplementary data

Supplementary Data are available at NAR Online.

Acknowledgements

We thank the Beamline BL19U1 staff at the Shanghai Synchrotron Radiation facility for X-ray data collection. This work was supported by National Natural Science Foundation of China (Grant Nos. 32171295 and 32071277), Natural Science Foundation of Hebei province (Grant Nos. C2022201025 and C2020201030), Hebei Educational committee Foundation (Grant No. ZD2020183), Interdisciplinary Research Program of Natural Science of Hebei University (No. DXK202006, DXK202007), and Hebei Province Foundation for Returned Overseas Chinese Scholars (C20200303).

Author contributions: X.L. designed and administrated the project. Y.M., J.W., X.H., Y.L., S.Z., L.A., Q.Y., F.N., H.W., B.A. and X.T. performed the experiments. Z.Y., X.Y., C.W. and X.L. analyzed the data. C.W., X.Y. and X.L. wrote the manuscript.

Funding

National Natural Science Foundation of China [32071277, 32171295]. Funding for open access charge: Natural Science Foundation of China.

Conflict of interest statement

None declared.

References

1. Tomecki,R., Sikorski,P.J. and Zakrzewska-Placzek,M. (2017) Comparison of preribosomal RNA processing pathways in yeast, plant and human cells - focus on coordinated action of endo- and exoribonucleases. *FEBS Lett.*, **591**, 1801–1850.
2. Pecoraro,A., Pagano,M., Russo,G. and Russo,A. (2021) Ribosome biogenesis and cancer: overview on ribosomal proteins. *Int. J. Mol. Sci.*, **22**, 5496.
3. Aubert,M., O'Donohue,M.F., Lebaron,S. and Gleizes,P.E. (2018) Pre-ribosomal RNA processing in Human cells: from mechanisms to congenital diseases. *Biomolecules*, **8**, 123.
4. Gilles,A., Frechin,L., Natchiar,K., Biondani,G., Loeffelholz,O.V., Holvec,S., Malaval,J.L., Winum,J.Y., Klaholz,B.P. and Peyron,J.F. (2020) Targeting the Human 80S ribosome in cancer: from structure to function and drug design for innovative adjuvant therapeutic strategies. *Cells*, **9**, 629.
5. Narla,A. and Ebert,B.L. (2010) Ribosomopathies: human disorders of ribosome dysfunction. *Blood*, **115**, 3196–3205.
6. Sloan,K.E., Mattijssen,S., Lebaron,S., Tollervey,D., Pruijn,G.J.M. and Watkins,N.J. (2013) Both endonucleolytic and exonucleolytic cleavage mediate ITS1 removal during human ribosomal RNA processing. *J. Cell Biol.*, **200**, 577–588.
7. Anger,A.M., Armache,J.P., Berninghausen,O., Habeck,M., Subklewe,M., Wilson,D.N. and Beckmann,R. (2013) Structures of the human and Drosophila 80S ribosome. *Nature*, **497**, 80–85.
8. Henras,A.K., Soudet,J., Gerus,M., Lebaron,S., Caizergues-Ferrer,M., Mougin,A. and Henry,Y. (2008) The post-transcriptional steps of eukaryotic ribosome biogenesis. *Cell. Mol. Life Sci.*, **65**, 2334–2359.
9. Tomecki,R., Labno,A., Drazkowska,K., Cysewski,D. and Dziembowski,A. (2015) hUTP24 is essential for processing of the human rRNA precursor at site A1, but not at site A0. *Rna Biol.*, **12**, 1010–1029.
10. Rouquette,J., Choesmel,V. and Gleizes,P.E. (2005) Nuclear export and cytoplasmic processing of precursors to the 40S ribosomal subunits in mammalian cells. *EMBO J.*, **24**, 2862–2872.
11. Wells,G.R., Weichmann,F., Colvin,D., Sloan,K.E., Kudla,G., Tollervey,D., Watkins,N.J. and Schneider,C. (2016) The PIN domain endonuclease Utp24 cleaves pre-ribosomal RNA at two coupled sites in yeast and humans. *Nucleic Acids Res.*, **44**, 5399–5409.
12. Preti,M., O'Donohue,M.F., Montel-Lehry,N., Bortolin-Cavaille,M.L., Choesmel,V. and Gleizes,P.E. (2013) Gradual processing of the ITS1 from the nucleolus to the cytoplasm during synthesis of the human 18S rRNA. *Nucleic Acids Res.*, **41**, 4709–4723.
13. Montellese,C., Montel-Lehry,N., Henras,A.K., Kutay,U., Gleizes,P.E. and O'Donohue,M.F. (2017) Poly(A)-specific ribonuclease is a nuclear ribosome biogenesis factor involved in human 18S rRNA maturation. *Nucleic Acids Res.*, **45**, 6822–6836.
14. Widmann,B., Wandrey,F., Badertscher,L., Wyler,E., Pfannstiel,J., Zemp,I. and Kutay,U. (2012) The kinase activity of human Rio1 is required for final steps of cytoplasmic maturation of 40S subunits. *Mol. Biol. Cell*, **23**, 22–35.
15. Zuo,Y. and Deutscher,M.P. (2001) Exoribonuclease superfamilies: structural analysis and phylogenetic distribution. *Nucleic Acids Res.*, **29**, 1017–1026.
16. Horio,T., Murai,M., Inoue,T., Hamasaki,T., Tanaka,T. and Ohgi,T. (2004) Crystal structure of human ISG20, an interferon-induced antiviral ribonuclease. *FEBS Lett.*, **577**, 111–116.
17. Coute,Y., Kindbeiter,K., Belin,S., Dieckmann,R., Duret,L., Bezin,L., Sanchez,J.C. and Diaz,J.J. (2008) ISG20L2, a novel vertebrate nucleolar exoribonuclease involved in ribosome biogenesis. *Mol. Cell. Proteomics*, **7**, 546–559.
18. Eppens,N.A., Faber,A.W., Rondaij,M., Jahangir,R.S., van Hemert,S., Vos,J.C., Venema,J. and Raue,H.A. (2002) Deletions in the S1 domain of Rrp5p cause processing at a novel site in ITS1 of yeast pre-rRNA that depends on Rex4p. *Nucleic Acids Res.*, **30**, 4222–4231.
19. Degols,G., Eldin,P. and Mechti,N. (2007) ISG20, an actor of the innate immune response. *Biochimie*, **89**, 831–835.
20. Weiss,C.M., Trobaugh,D.W., Sun,C.Q., Lucas,T.M., Diamond,M.S., Ryman,K.D. and Klimstra,W.B. (2018) The interferon-induced exonuclease ISG20 exerts antiviral activity through upregulation of type I interferon response proteins. *mSphere*, **3**, e00209-18.
21. Xu,T.B., Ruan,H.L., Gao,S., Liu,J.C., Liu,Y.N., Song,Z.S., Cao,Q., Wang,K.S., Bao,L., Liu,D., *et al.* (2020) ISG20 serves as a potential biomarker and drives tumor progression in clear cell renal cell carcinoma. *Aging*, **12**, 1789–1808.
22. Montano,M.M., Wittmann,B.M. and Bianco,N.R. (2000) Identification and characterization of a novel factor that regulates quinone reductase gene transcriptional activity. *J. Biol. Chem.*, **275**, 34306–34313.
23. Krishnamurthy,N., Ngam,C.R., Berdis,A.J. and Montano,M.M. (2011) The exonuclease activity of hPMC2 is required for transcriptional regulation of the QR gene and repair of estrogen-induced abasic sites. *Oncogene*, **30**, 4731–4739.
24. Lee,J.H., Koh,Y.A., Cho,C.K., Lee,S.J., Lee,Y.S. and Bae,S. (2005) Identification of a novel ionizing radiation-induced nuclease, AEN, and its functional characterization in apoptosis. *Biochem. Bioph. Res. Commun.*, **337**, 39–47.
25. Kawase,T., Ichikawa,H., Ohta,T., Nozaki,N., Tashiro,F., Ohki,R. and Taya,Y. (2008) p53 target gene AEN is a nuclear exonuclease required for p53-dependent apoptosis. *Oncogene*, **27**, 3797–3810.
26. Ma,K., Luo,M., Xie,G., Wang,X., Li,Q., Gao,L., Yu,H. and Yu,X. (2022) Ribosomal RNA regulates chromosome clustering during mitosis. *Cell Discov.*, **8**, 51.
27. Galvis,A.E., Fisher,H.E., Nitta,T., Fan,H. and Camerini,D. (2014) Impairment of HIV-1 cDNA synthesis by DBR1 knockdown. *J. Virol.*, **88**, 7054–7069.
28. Minor,W., Cymborowski,M., Otwinowski,Z. and Chruszcz,M. (2006) HKL-3000: the integration of data reduction and structure solution - from diffraction images to an initial model in minutes. *Acta Crystallogr. D Struct. Biol.*, **62**, 859–866.
29. McCoy,A.J., Grosse-Kunstleve,R.W., Adams,P.D., Winn,M.D., Storoni,L.C. and Read,R.J. (2007) Phaser crystallographic software. *J. Appl. Crystallogr.*, **40**, 658–674.

30. Langer,G., Cohen,S.X., Lamzin,V.S. and Perrakis,A. (2008) Automated macromolecular model building for X-ray crystallography using ARP/wARP version 7. *Nat. Protoc.*, **3**, 1171–1179.
31. Adams,P.D., Afonine,P.V., Bunkoczi,G., Chen,V.B., Davis,I.W., Echols,N., Headd,J.J., Hung,L.W., Kapral,G.J., Grosse-Kunstleve,R.W., *et al.* (2010) PHENIX: a comprehensive Python-based system for macromolecular structure solution. *Acta Crystallogr. D Biol. Crystallogr.*, **66**, 213–221.
32. Emsley,P., Lohkamp,B., Scott,W.G. and Cowtan,K. (2010) Features and development of Coot. *Acta Crystallogr D*, **66**, 486–501.
33. Ishikawa,H., Yoshikawa,H., Izumikawa,K., Miura,Y., Taoka,M., Nobe,Y., Yamauchi,Y., Nakayama,H., Simpson,R.J., Isobe,T., *et al.* (2017) Poly(A)-specific ribonuclease regulates the processing of small-subunit rRNAs in human cells. *Nucleic Acids Res.*, **45**, 3437–3447.
34. Tomecki,R., Kristiansen,M.S., Lykke-Andersen,S., Chlebowski,A., Larsen,K.M., Szczesny,R.J., Drazkowska,K., Pastula,A., Andersen,J.S., Stepien,P.P., *et al.* (2010) The human core exosome interacts with differentially localized processive RNases: hDIS3 and hDIS3L. *EMBO J.*, **29**, 2342–2357.
35. Prakash,V., Carson,B.B., Feenstra,J.M., Dass,R.A., Sekyrova,P., Hoshino,A., Petersen,J., Guo,Y., Parks,M.M., Kurylo,C.M., *et al.* (2019) Ribosome biogenesis during cell cycle arrest fuels EMT in development and disease. *Nat. Commun.*, **10**, 2110.
36. Chen,J., Liu,L., You,C., Gu,J., Ruan,W., Zhang,L., Gan,J., Cao,C., Huang,Y., Chen,X., *et al.* (2018) Structural and biochemical insights into small RNA 3' end trimming by Arabidopsis SDN1. *Nat. Commun.*, **9**, 3585.
37. Wu,M., Reuter,M., Lilie,H., Liu,Y., Wahle,E. and Song,H. (2005) Structural insight into poly(A) binding and catalytic mechanism of human PARN. *EMBO J.*, **24**, 4082–4093.
38. Zuo,Y., Zheng,H., Wang,Y., Chruszcz,M., Cymborowski,M., Skarina,T., Savchenko,A., Malhotra,A. and Minor,W. (2007) Crystal structure of RNase T, an exoribonuclease involved in tRNA maturation and end turnover. *Structure*, **15**, 417–428.
39. Cheng,Y. and Patel,D.J. (2004) Crystallographic structure of the nuclease domain of 3'hExo, a DEDDh family member, bound to rAMP. *J. Mol. Biol.*, **343**, 305–312.
40. Tang,T.T.L., Stowell,J.A.W., Hill,C.H. and Passmore,L.A. (2019) The intrinsic structure of poly(A) RNA determines the specificity of Pan2 and Caf1 deadenylases. *Nat. Struct. Mol. Biol.*, **26**, 433–442.
41. Jonas,S., Christie,M., Peter,D., Bhandari,D., Loh,B., Huntzinger,E., Weichenrieder,O. and Izaurralde,E. (2014) An asymmetric PAN3 dimer recruits a single PAN2 exonuclease to mediate mRNA deadenylation and decay. *Nat. Struct. Mol. Biol.*, **21**, 599–608.
42. Cheng,H.L., Lin,C.T., Huang,K.W., Wang,S.Y., Lin,Y.T., Toh,S.I. and Hsiao,Y.Y. (2018) Structural insights into the duplex DNA processing of TREX2. *Nucleic Acids Res.*, **46**, 12166–12176.
43. Hamdan,S., Carr,P.D., Brown,S.E., Ollis,D.L. and Dixon,N.E. (2002) Structural basis for proofreading during replication of the Escherichia coli chromosome. *Structure*, **10**, 535–546.
44. Pelletier,J., Thomas,G. and Volarevic,S. (2018) Ribosome biogenesis in cancer: new players and therapeutic avenues. *Nat. Rev. Cancer*, **18**, 51–63.
45. Molavi,G., Samadi,N. and Hosseingholi,E.Z. (2019) The roles of moonlight ribosomal proteins in the development of human cancers. *J. Cell. Physiol.*, **234**, 8327–8341.
46. Penzo,M., Montanaro,L., Trere,D. and Derenzini,M. (2019) The ribosome biogenesis-cancer connection. *Cells*, **8**, 55.
47. Yin,J.B., Lin,C., Jiang,M., Tang,X.B., Xie,D.L., Chen,J.W. and Ke,R.Q. (2021) CENPL, ISG20L2, LSM4, MRPL3 are four novel hub genes and may serve as diagnostic and prognostic markers in breast cancer. *Sci. Rep.*, **11**, 15610.
48. Chen,H.T., Li,Y.Y., Xiao,S.Y. and Guo,J.C. (2021) Identification of a five-immune gene model as an independent prognostic factor in hepatocellular carcinoma. *BMC Cancer*, **21**, 278.
49. Zhou,Y., Xu,B., Zhou,Y., Liu,J., Zheng,X., Liu,Y.T., Deng,H.F., Liu,M., Ren,X.B., Xia,J.C.A., *et al.* (2021) Identification of key genes with differential correlations in lung adenocarcinoma. *Front. Cell Dev. Biol.*, **9**, 675438.
50. Liu,Y., Deisenroth,C. and Zhang,Y. (2016) RP-MDM2-p53 pathway: linking ribosomal biogenesis and tumor surveillance. *Trends Cancer*, **2**, 191–204.
51. Lafita-Navarro,M.C. and Conacci-Sorrell,M. (2023) Nucleolar stress: from development to cancer. *Semin. Cell Dev. Biol.*, **136**, 64–74.
52. Wang,Z., Fan,M., Candas,D., Zhang,T.Q., Qin,L., Eldridge,A., Wachsmann-Hogiu,S., Ahmed,K.M., Chromy,B.A., Nantajit,D., *et al.* (2014) Cyclin B1/Cdk1 coordinates mitochondrial respiration for cell-cycle G2/M progression. *Dev. Cell*, **29**, 217–232.
53. Peter,M., Le Peuch,C., Labbe,J.C., Meyer,A.N., Donoghue,D.J. and Doree,M. (2002) Initial activation of cyclin-B1-cdc2 kinase requires phosphorylation of cyclin B1. *EMBO Rep.*, **3**, 551–556.
54. Belin,S., Beghin,A., Solano-Gonzalez,E., Bezin,L., Brunet-Manquat,S., Textoris,J., Prats,A.C., Mertani,H.C., Dumontet,C. and Diaz,J.J. (2009) Dysregulation of ribosome biogenesis and translational capacity is associated with tumor progression of human breast cancer cells. *PLoS One*, **4**, e7147.
55. Nagaraj,N., Wisniewski,J.R., Geiger,T., Cox,J., Kircher,M., Kelso,J., Paabo,S. and Mann,M. (2011) Deep proteome and transcriptome mapping of a human cancer cell line. *Mol. Syst. Biol.*, **7**, 548.
56. An,B.C., Hong,S., Park,H.J., Kim,B.K., Ahn,J.Y., Ryu,Y., An,J.H. and Chung,M.J. (2019) Anti-colorectal cancer effects of probiotic-derived p8 protein. *Genes*, **10**, 624.
57. Hu,A., Huang,J.J., Zhang,J.F., Dai,W.J., Li,R.L., Lu,Z.Y., Duan,J.L., Li,J.P., Chen,X.P., Fan,J.P., *et al.* (2017) Curcumin induces G2/M cell cycle arrest and apoptosis of head and neck squamous cell carcinoma in vitro and in vivo through ATM/Chk2/p53-dependent pathway. *Oncotarget*, **8**, 50747–50760.
58. Rizzotto,D., Englmaier,L. and Villunger,A. (2021) At a crossroads to cancer: how p53-induced cell fate decisions secure genome integrity. *Int. J. Mol. Sci.*, **22**, 10883.
59. Liu,L., Zhang,P., Bai,M., He,L., Zhang,L., Liu,T., Yang,Z., Duan,M., Liu,M., Liu,B., *et al.* (2019) p53 upregulated by HIF-1alpha promotes hypoxia-induced G2/M arrest and renal fibrosis in vitro and in vivo. *J. Mol. Cell Biol.*, **11**, 371–382.
60. Kastan,M.B. and Kuerbitz,S.J. (1993) Control of G1 arrest after DNA damage. *Environ. Health Perspect.*, **101**, 55–58.
61. Linke,S.P., Clarkin,K.C., Di Leonardo,A., Tsou,A. and Wahl,G.M. (1996) A reversible, p53-dependent G0/G1 cell cycle arrest induced by ribonucleotide depletion in the absence of detectable DNA damage. *Genes Dev.*, **10**, 934–947.
62. Pellegata,N.S., Antoniono,R.J., Redpath,J.L. and Stanbridge,E.J. (1996) DNA damage and p53-mediated cell cycle arrest: a reevaluation. *Proc. Nat. Acad. Sci. U.S.A.*, **93**, 15209–15214.
63. Brown,L., Boswell,S., Raj,L. and Lee,S.W. (2007) Transcriptional targets of p53 that regulate cellular proliferation. *Crit. Rev. Eukar. Gene*, **17**, 73–85.

Received: November 22, 2022. **Revised:** December 3, 2023. **Editorial Decision:** December 6, 2023. **Accepted:** December 10, 2023